Geophysical Journal International

Geophys. J. Int. (2021) **225,** 926–949
Advance Access publication 2021 January 13
GJI Seismology

doi: 10.1093/gji/ggab017

Double-difference seismic attenuation tomography method and its application to The Geysers geothermal field, California

Hao Guo and Clifford Thurber

Department of Geoscience, University of Wisconsin-Madison, 1215 *W. Dayton St., Madison, WI* 53706, *USA. E-mail:* hao.guo@wisc.edu

Accepted 2021 January 11. Received 2020 December 16; in original form 2020 August 1

SUMMARY

Knowledge of attenuation structure is important for understanding subsurface material properties. We have developed a double-difference seismic attenuation (DDQ) tomography method for high-resolution imaging of 3-D attenuation structure. Our method includes two main elements, the inversion of event-pair differential t^* (dt^*) data and 3-D attenuation tomography with the dt^* data. We developed a new spectral ratio method that jointly inverts spectral ratio data from pairs of events observed at a common set of stations to determine the dt^* data. The spectral ratio method cancels out instrument and site response terms, resulting in more accurate dt^* data compared to absolute t^* from traditional methods using individual spectra. Synthetic tests show that the inversion of dt^* data using our spectral ratio method is robust to the choice of source model and a moderate degree of noise. We modified an existing velocity tomography code so that it can invert dt^* data for 3-D attenuation structure. We applied the new method to The Geyser geothermal field, California, which has vapour-dominated reservoirs and a long history of water injection. A new *Qp* model at The Geysers is determined using *P*-wave data of earthquakes in 2011, using our updated earthquake locations and *Vp* model. By taking advantage of more accurate dt^* data and the cancellation of model uncertainties along the common paths outside of the source region, the DDQ tomography method achieves higher resolution, especially in the earthquake source regions, compared to the standard tomography method using t^* data. This is validated by both the real and synthetic data tests. Our *Qp* and *Vp* models show consistent variations in a normal temperature reservoir that can be explained by variations in fracturing, permeability and fluid saturation and/or steam pressure. A prominent low-*Qp* and Vp zone associated with very active seismicity is imaged within a high temperature reservoir at depths below 2 km. This anomalous zone is likely partially saturated with injected fluids.

Key words: Body waves; Seismic attenuation; Seismic tomography.

1 INTRODUCTION

Compared to seismic compressional and shear wave velocities (*Vp* and *Vs*), seismic attenuation, represented by seismic quality factor *Q*, is more sensitive to rock properties related to pores, cracks, fractures and fluids. A popular way to determine subsurface 3-D *Q* structure is to invert observed earthquake spectra for path attenuation terms, t^*, from a set of earthquakes at a set of stations and then perform 3-D *Q* tomography with the obtained t^* data. The recorded seismogram is affected by two types of attenuation, intrinsic attenuation and scattering attenuation (Sato & Fehler 2009). Intrinsic attenuation is the energy loss of seismic waves when passing through rocks. Intrinsic attenuation is highly influenced by rock porosity, pore shape, pore density, permeability, saturation, confining pressure and pore pressure (O'Connell & Budiansky 1977; Winkler & Nur 1979; Peacock *et al.* 1994). Intrinsic attenuation is weekly dependent on frequency within the seismic frequency band according to lab experiments (e.g. Fail & Jackson 2015) and seismic observations (e.g. Pozgay *et al.* 2009; Wei & Wiens 2018). Scattering attenuation is the energy redistribution of seismic waves when being converted, reflected, or refracted by small-scale scatterers. Scattering attenuation can be frequency dependent, depending on the size of scatterers relative to the wavelength (Frankel 1991).

Most standard *Q* tomography methods use absolute t^* data that are inverted from single spectrum data for individual earthquakes observed at individual stations (Scherbaum 1990; Rietbrock 1996; Thurber & Eberhart-Phillips 1999; Rietbrock 2001; Eberhart-Phillips & Chadwick 2002; Pozgay *et al.* 2009; Liu *et al.* 2014) or for groups of earthquakes observed at groups of stations (Bennington *et al.* 2008; Bisrat *et al.* 2014; Ohlendorf *et al.* 2014). Since the inversion of t^* data is coupled to instrument response, site response and source parameters, some methods using spectral ratio data have been used to remove some coupling effects to determine more accurate differential t^* (dt^*) data, which also can be used to estimate *Q* structure. There are four kinds of spectral ratio methods, including station-pair, event-pair, phase-pair and event pair-station pair (or double-pair) spectral ratios. The station-pair method takes the ratio of spectra from individual earthquakes at pairs of stations, which can remove the source spectrum. The phase-pair method takes the ratio of two different types of waves (e.g. *P* and *S*) from individual earthquakes at individual stations. Roth *et al.* (1999) have a clear discussion of the station-pair and phase-pair spectral ratio methods. The event-pair method takes the ratio of spectra from pairs of events at individual stations, which can remove the instrument response and site response. Many studies (e.g. Imanishi & Ellsworth 2006; Abercrombie 2014; Liu *et al.* 2014) used event-pair spectral ratio data to estimate corner frequency and stress drop for co-located earthquakes from direct or coda waves but did not solve for path attenuation, which could be removed due to the overlapping ray paths. Shiina *et al.* (2018) and Kriegerowski *et al.* (2019) used event-pair spectral ratio data to directly solve for average path attenuation in the earthquake source region. The double-pair method uses spectral ratio data from pairs of earthquakes at pairs of stations to invert for dt^* and then fit dt^* data for all pairs of events in a cluster to estimate the average attenuation in the fault zone (Blakeslee *et al.* 1989). The method of Blakeslee *et al.* (1989) has a strict requirement on the distribution of events and stations relative to the fault zone. Zhang *et al.* (2007) used double-pair spectral ratio data to obtain dt^* data, analogous to the method of Blakeslee *et al.* (1989), but then performed a tomographic inversion to determine 3-D Q structure.

In this paper, we develop a double-difference (DD) attenuation (DDQ) tomography method. Our DDQ tomography method includes two main parts: (1) extracting dt^* data using a new event-pair spectral ratio method, and (2) performing 3-D Q tomography with the obtained dt^* data. Our spectral ratio method jointly inverts for all source and attenuation parameters using spectral ratios from pairs of events observed at common stations. Instead of using dt^* data to determine the average attenuation in the source region, which requires special distributions of ray paths (Shiina *et al.* 2018; Kriegerowski *et al.* 2019), we use them for a tomographic inversion for 3-D Q structure without such a requirement. Compared to the standard Q tomography method using absolute t^* data, our DDQ tomography method can determine higher resolution Q structure for two reasons: (1) higher quality of dt^* data from spectral ratio inversions; and (2) event-pair dt^*data can cancel out the effect of model uncertainties along the common ray path outside the source region, so that the source-region structure can be better imaged.

We first tested our spectral ratio method with noise-free and noise-added synthetic data. Then, we applied our DDQ tomography method to The Geysers geothermal field, the largest geothermal field in the world, and tested its performance with synthetic and real data. We also updated the earthquake locations and 3-D Vp model. We selected The Geysers for a number of reasons. (1) The Geysers has vapour-dominated reservoirs and has a long history of water injection to enhance the steam production associated with very active induced seismicity (Hartline *et al.* 2016). Due to high sensitivity of attenuation to saturation conditions of rocks, The Geysers is an ideal area to test whether our DDQ tomography method can image subsurface steam reservoirs and water injection zones. (2) The cancellation of site response using our spectral ratio method is particularly important for The Geysers due to the very strong site response there (Romero *et al.* 1997). (3) The seismic network at The Geysers is relatively dense. A 34-station seismic network has been operated by Lawrence Berkeley National Laboratory (Majer & Peterson 2007) and the waveform data are available from the Northern California Earthquake Data Center. (4) Many velocity and Q tomography studies have been done at The Geysers (O'Connell & Johnson 1991; Zucca *et al.* 1994; Romero *et al.* 1995; Julian *et al.* 1996; Romero *et al.* 1997; Gritto *et al.* 2013; Jeanne *et al.* 2015; Lin & Wu 2018; Hutchings *et al.* 2019; Gritto *et al.* 2020). We can compare our new Q model with previous models to see if their overall structures are similar and if our new model has higher resolution in earthquake source regions.

In this study, we assume frequency independent Q. Since previous Q tomography studies at The Geysers also assumed frequency independent Q (Zucca *et al.* 1994; Romero *et al.* 1997; Hutchings *et al.* 2019), we can directly compare our Q model with previous Q models. However, frequency dependent Q may be the case for The Geysers, which is dominated by steam and fluid filled pores and fractures. Eberhart-Phillips *et al.* (2014) show that, to first order, if Q is frequency dependent, that is, $Q = Q_0 \;\; f^{\alpha}$, where α ranges from 0 to 1, then the Q model obtained by inverting t^* values assuming frequency independence approximately differs by a multiplicative scale factor from the correct frequency dependent Q model (Q_0). This means that the pattern of Q variations is correct but the absolute values of Q are not. This should also be the case for inverting dt^* data. Furthermore, in a previous Q tomography study at The Geysers, Romero *et al.* (1997) argued that assuming frequency independent Q was appropriate.

2 METHODOLOGY

In this section, we first describe the methodology of extracting absolute t^* data using the single spectrum method and dt^* data using the spectral ratio method. We then describe the methodology of DDQ tomography with absolute t^* and dt^* data.

2.1 Fitting event-pair spectral ratio for dt^*

The observed amplitude spectrum $A_k^i(f)$ of an earthquake i at station k for frequency f can be expressed as (Scherbaum 1990)

$$A_k^i(f) = S_i(f)\, I_k(f)\, R_k(f)\, B_k^i(f) \tag{1}$$

where $S_i(f)$ is the source spectrum, $I_k(f)$ is the instrument response, $R_k(f)$ is the local site amplification (site response) and $B_k^i(f)$is the attenuation spectrum that describes the wave amplitude loss along the ray path. The source spectrum for earthquake i can be expressed as

$$S_i(f) = \frac{\Omega_0^{ik}}{1 + \left(f/f_c^i\right)^{\gamma}} \tag{2}$$

where Ω_0^{ik} is the zero-frequency spectral level for earthquake i at station k, accounting for the effects of radiation pattern and geometric spreading, f_c^i is the source corner frequency and γ represents the high-frequency decay factor, which is 2 for a Brune ω^2 type source model (Brune 1970). Assuming frequency independent attenuation, the attenuation spectrum can be expressed as

$$B_k^i(f) = e^{-\pi f t_{ik}^*} \tag{3}$$

where t_{ik}^* is the whole path attenuation operator.

With eqs (2) and (3), the velocity amplitude spectrum (eq. 1) can be expressed as

$$A_k^i(f) = I_k(f)\, R_k(f)\, \frac{\Omega_0^{ik}}{1 + \left(f/f_c^i\right)^{\gamma}}\, e^{-\pi f t_{ik}^*} \tag{4}$$

where $R_k(f)$, Ω_0^{ik}, f_c^i and t_{ik}^* are the unknowns, and $I_k(f)$ is known in principle. This is the basic equation for all the methods that

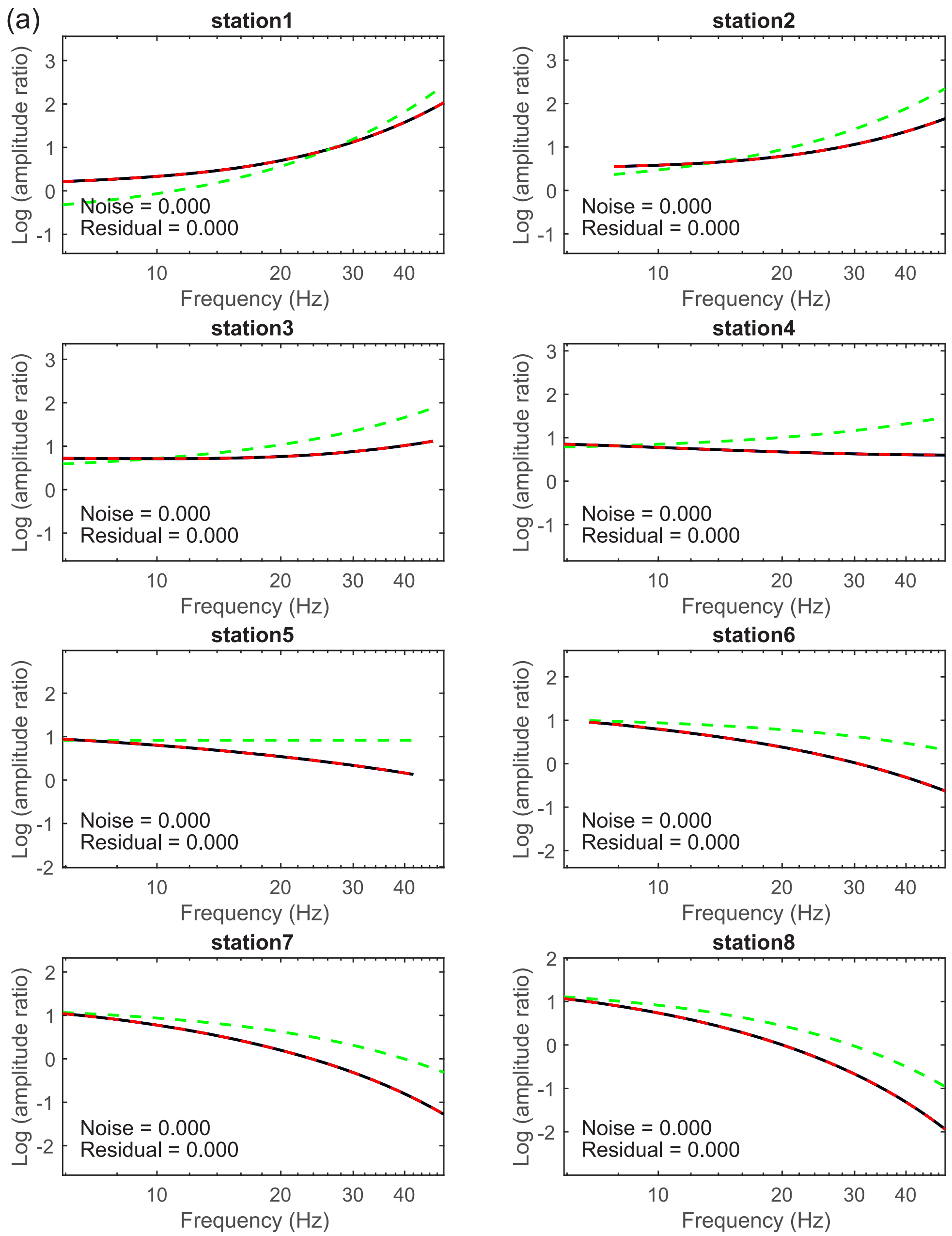

Figure 1. (a) Noise-free and (b) noise-added synthetic spectral ratio data in the natural logarithm domain as a function of frequency at eight stations. Black solid lines represent the input noise-free and noise-added data used for inversions. Green and red dashed lines represent the modelled spectral ratio data using the initial and inverted parameters, respectively. In (a), the black solid and red dashed lines overlap due to the perfect data fit for noise-free synthetic tests. In (b), the blue lines represent the true spectral ratio data. The noise (the rms value of the differences between the input and true spectral ratios for all the frequencies used) and final data residual after the inversion at each station are labelled.

use single spectrum data to obtain t^* data for standard Q tomography (e.g. Scherbaum 1990; Rietbrock 1996; Thurber & Eberhart-Phillips 1999; Rietbrock 2001; Eberhart-Phillips & Chadwick 2002; Bisrat *et al.* 2014). Hereafter, the methods using single spectra to obtain t^* data are collectively termed the single spectrum method.

Considering two earthquakes i and j recorded by a common station k, the ratio of their amplitude spectra, $R_{A_k}(f)$, can be expressed as

$$R_{A_k}(f) = \frac{A_k^i(f)}{A_k^j(f)} = \frac{\Omega_0^{ik}}{\Omega_0^{jk}} \frac{1 + \left(f/f_c^j\right)^\gamma}{1 + \left(f/f_c^i\right)^\gamma} e^{-\pi f\left(t_{ik}^* - t_{jk}^*\right)} \tag{5}$$

Taking the natural logarithm of eq. (5), we obtain

$$\begin{aligned} \log\left(R_{A_k}(f)\right) &= \log\left(\frac{\Omega_0^{ik}}{\Omega_0^{jk}}\right) + \log\left(1 + \left(f/f_c^j\right)^\gamma\right) \\ &\quad - \log\left(1 + \left(f/f_c^i\right)^\gamma\right) - \pi f\left(t_{ik}^* - t_{jk}^*\right) \\ &= \log\left(R_{\Omega_k}\right) + \log\left(1 + \left(f/f_c^j\right)^\gamma\right) \\ &\quad - \log\left(1 + \left(f/f_c^i\right)^\gamma\right) - \pi f dt_k^* \end{aligned} \tag{6}$$

where R_{Ω_k} is the ratio of low-frequency spectral levels at station k and $dt_k^* = t_{ik}^* - t_{jk}^*$ is the event-pair differential t^* at station k. In this equation, R_{Ω_k}, f_c^i, f_c^j and dt_k^* are the only unknowns because the

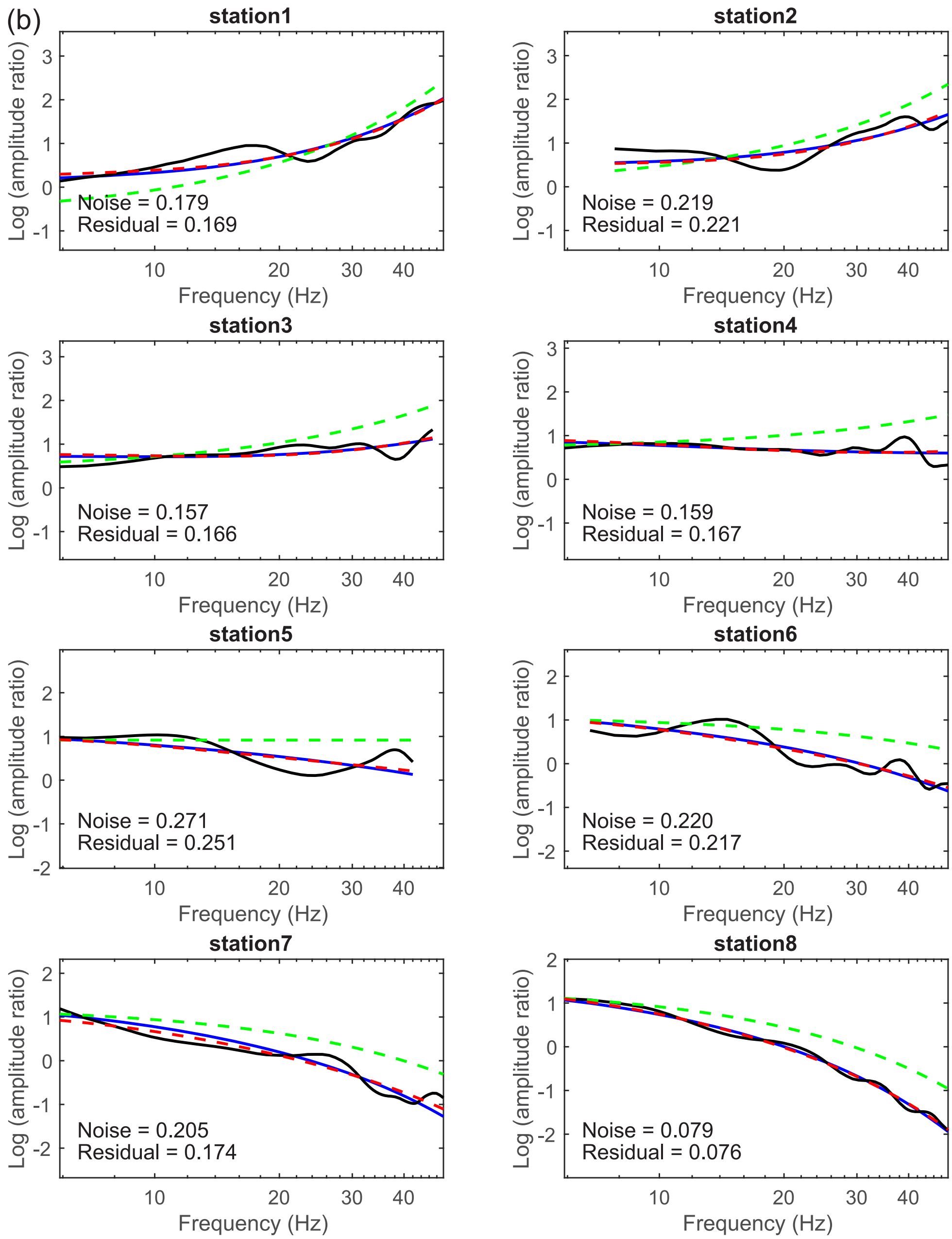

Figure 1. (*Continued.*)

instrument response and site response terms cancel out. Since the relationship between the spectral ratio and the source parameters is nonlinear, the Levenberg–Marquardt (LM) method (Aster *et al.* 2019), an iterative, damped least squares method, can be used to solve the spectral ratio equation for the unknowns. First, we use a truncated Taylor series approximation to linearize the difference between observed and calculated values, r_k, for eq. (6), as follows

$$\begin{aligned} r_k &= \log\left(R_{A_k}^{\mathrm{obs}}\right) - \log\left(R_{A_k}^{\mathrm{cal}}\right) \\ &= \frac{\partial\left[\log\left(R_{A_k}\right)\right]}{\partial f_c^i}\Delta f_c^i + \frac{\partial\left[\log\left(R_{A_k}\right)\right]}{\partial f_c^j}\Delta f_c^j \\ &\quad + \frac{\partial\left[\log\left(R_{A_k}\right)\right]}{\partial R_{\Omega_k}}\Delta R_{\Omega_k} + \frac{\partial\left[\log\left(R_{A_k}\right)\right]}{\partial dt_k^*}\Delta dt_k^* \end{aligned} \tag{7}$$

for a given estimate of the parameter values. The partial derivatives of the spectral ratio with respect to the unknowns in eq. (7) can be expressed as

$$\frac{\partial\left[\log\left(R_{A_k}\right)\right]}{\partial f_c^i} = \gamma\left(\frac{1}{f^\gamma} + \frac{1}{\left(f_c^i\right)^\gamma}\right)^{-1}\left(f_c^i\right)^{-\gamma-1} \tag{7a}$$

$$\frac{\partial\left[\log\left(R_{A_k}\right)\right]}{\partial f_c^j} = -\gamma\left(\frac{1}{f^\gamma} + \frac{1}{\left(f_c^j\right)^\gamma}\right)^{-1}\left(f_c^j\right)^{-\gamma-1} \tag{7b}$$

$$\frac{\partial\left[\log\left(R_{A_k}\right)\right]}{\partial R_{\Omega_k}} = \frac{1}{R_{\Omega_k}} \tag{7c}$$

$$\frac{\partial\left[\log\left(R_{A_k}\right)\right]}{\partial dt_k^*} = -\pi f \tag{7d}$$

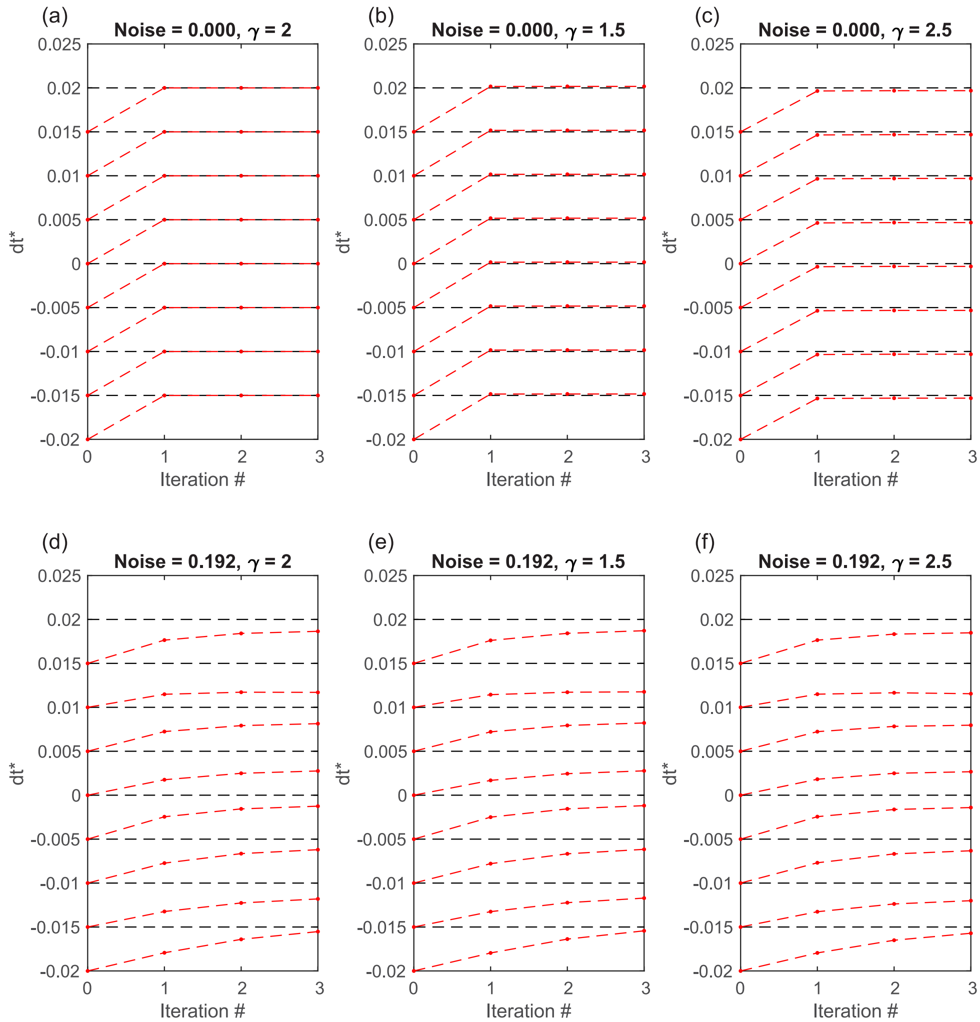

Figure 2. The evolution of inverted dt^* with iterations for (a)–(c) noise-free and (d)–(f) noise-added synthetic tests that generated synthetic spectral ratio data with γ values of (a) and (d) 2, (b) and (e) 1.5, and (c) and (f) 2.5 and used a γ value of 2 for inversions. Each black dashed line represents the true dt^* at each station. Red dots connected by red dashed lines represent the inverted dt^* after each iteration except for the dots at iteration 0 that represent the initial dt^*.

We solve the linear system of eq. (7) for one event pair recorded by n stations as follows,

$$\Delta \boldsymbol{m} = \left(\boldsymbol{J}(\boldsymbol{m})^T \boldsymbol{J}(\boldsymbol{m}) + \lambda \boldsymbol{I}\right)^{-1} \boldsymbol{J}(\boldsymbol{m})^T \boldsymbol{r}(\boldsymbol{m}) \tag{8}$$

where $\Delta \boldsymbol{m}$ is the vector of perturbations of the $2n + 2$ unknowns ($\boldsymbol{m}$) including n R_Ω, n dt^* and two f_c, $\boldsymbol{J}(\boldsymbol{m})$ is the matrix of partial derivatives of spectral ratios for all usable frequencies with respect to all unknowns (the Jacobian matrix) and $\boldsymbol{r}(\boldsymbol{m})$ is the vector of the residuals between the observed and calculated spectral ratios for all usable frequencies. The Jacobian matrix and residual vector are weighted based on the quality (signal-to-noise ratio, SNR) of each datum. The weighted Jacobian matrix is further processed with column scaling to avoid the large contrast of sensitivities of some parameters. A damping parameter λ is used to stabilize the inversion system to facilitate the convergence of the solution. We search for a λ value that can yield a moderate condition number for the inversion system, which is calculated by dividing the maximum singular value by the minimum singular value and used as an indicator of the stability of the least-squares inversion (Aster *et al.* 2019).

The initial parameters $\boldsymbol{m}_0$ can be obtained from the inversion using a single spectrum method to solve for Ω_0, t^* and f_c (e.g. Bisrat *et al.* 2014). At each iteration i, we update the model, $\boldsymbol{m}_i = \boldsymbol{m}_{i-1} + \Delta \boldsymbol{m}$, recalculate the residual vector and Jacobian matrix, and determine the new perturbation $\Delta \boldsymbol{m}$. The inversion stops when the norm of the residual vector no longer decreases significantly.

2.2 DDQ tomography

Assuming frequency independent attenuation, the whole path attenuation operator t^* from event i to station k can expressed as a path integral as follows (Scherbaum 1990),

$$t^*_{ik} = \frac{t_{ik}}{Q_{ik}} = \int_i^k u Q^{-1} dl + s_k \tag{9}$$

where t_{ik} is the traveltime, Q_{ik} is the whole path dimensionless quality factor Q along the ray path, u represents the slowness (the reciprocal of velocity), dl is an element of path length and s_k is a station correction term accounting for unmodelled structure near the surface below station k. Solving for the attenuation structure is a standard seismic tomography problem analogous to solving for seismic velocity structure with source locations fixed. Although eq. (9) can be solved directly for Q^{-1}, we determine the perturbations of

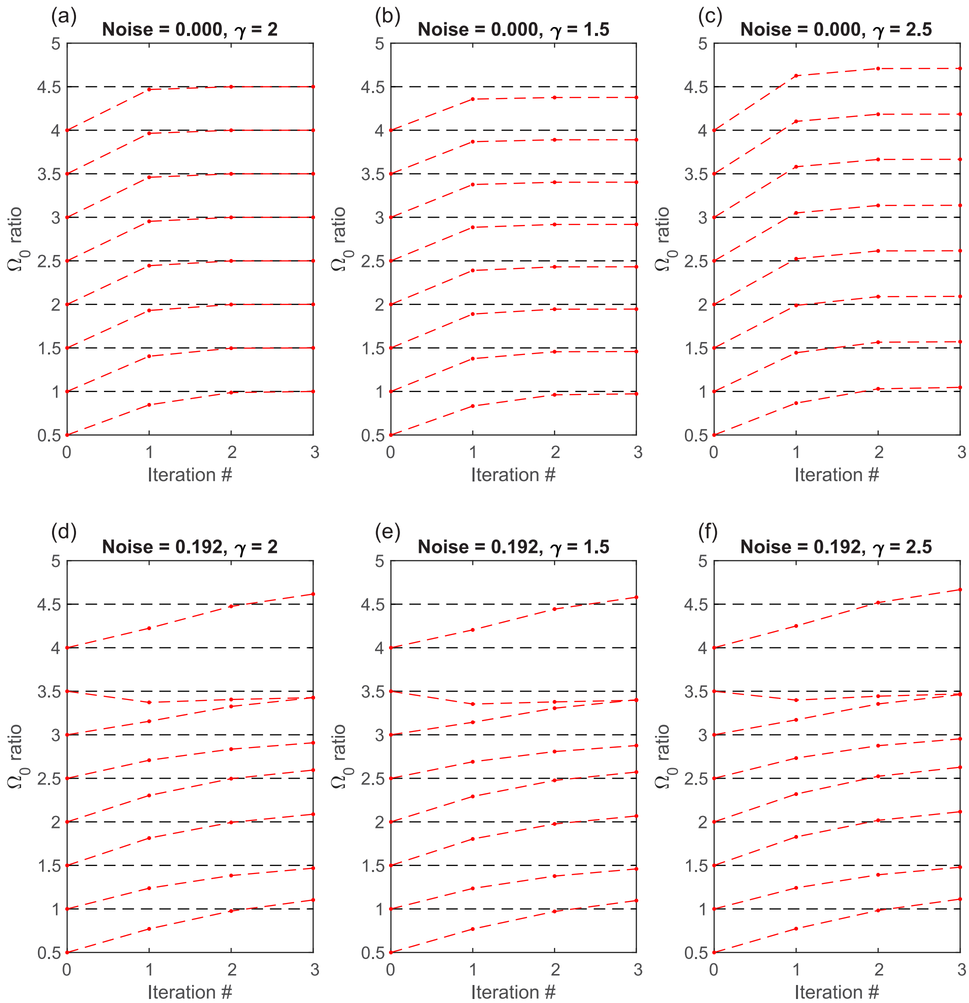

Figure 3. The evolution of inverted Ω_0 ratio with iterations for (a)–(c) noise-free and (d)–(f) noise-added synthetic tests that generated synthetic spectral ratio data with γ values of (a) and (d) 2, (b) and (e) 1.5, and (c) and (f) 2.5 and used a γ value of 2 for inversions. Each black dashed line represents the true Ω_0 ratio at each station. Red dots connected by red dashed lines represent the inverted Ω_0 ratios after each iteration except for the dots at iteration 0 that represent the initial Ω_0 ratios.

Q^{-1} ($\Delta(Q^{-1})$) and s_k (Δs_k) relative to a model estimate by

$$r_{ik} = \left(t^*_{ik}\right)^{\text{obs}} - \left(t^*_{ik}\right)^{\text{cal}} = \int_i^k u\Delta(Q^{-1})dl + \Delta s_k \tag{10}$$

where r_{ik} is the difference between the observed and calculated t^* values.

By subtracting a similar equation for event j observed at station k from eq. (10), we have

$$\begin{aligned} dr^k_{ij} &= r_{ik} - r_{jk} \\ &= \left[\left(t^*_{ik}\right)^{\text{obs}} - \left(t^*_{ik}\right)^{\text{cal}}\right] - \left[\left(t^*_{jk}\right)^{\text{obs}} - \left(t^*_{jk}\right)^{\text{cal}}\right] \\ &= \left[\left(t^*_{ik}\right)^{\text{obs}} - \left(t^*_{jk}\right)^{\text{obs}}\right] - \left[\left(t^*_{ik}\right)^{\text{cal}} - \left(t^*_{jk}\right)^{\text{cal}}\right] \\ &= \left(dt^*_{ijk}\right)^{\text{obs}} - \left(dt^*_{ijk}\right)^{\text{cal}} \\ &= \int_i^k u\Delta(Q^{-1})dl - \int_j^k u\Delta\left(Q^{-1}\right)dl \end{aligned} \tag{11}$$

where dr^k_{ij} is the difference between the observed and calculated dt^* values, that is, the double difference. The observed dt^* data can be obtained either from the spectral ratio inversion or by differencing absolute t^* data from the single spectrum inversion. Hereafter, dt^* obtained by differencing absolute t^* data from the single spectrum inversion is termed single spectrum dt^* and dt^* obtained from the spectral ratio inversion is termed spectral ratio dt^*.

We modified a 3-D seismic velocity tomography code tomoTD (Guo & Zhang 2017; Guo *et al.* 2018a), which can handle inversions with absolute arrival time data only, differential arrival time data only, or a combination of absolute and differential data, to determine 3-D Q structure with absolute t^* (eq. 10) and/or dt^* (eq. 11) data. tomoTD was developed based on the DD velocity tomography code tomoDD of Zhang & Thurber (2003). For solving the system of equations including absolute data and event-pair differential data, the major difference between tomoTD and tomoDD is the inclusion of station correction terms in the inversion. As with DD velocity tomography (Zhang & Thurber 2003), eqs (10) and (11) with a smoothing constraint applied to the model perturbations are solved with the damped least-squares solver LSQR (Paige & Saunders 1982). The inclusion of damping and smoothing, which are used to stabilize the inversion, makes the inversion nonlinear and thus multiple iterations are required. We can start the inversion by applying higher weight to absolute t^*data to establish the large-scale Q structure, then weight single spectrum dt^* data more heavily to refine the structure in the source regions, and finally weight the more

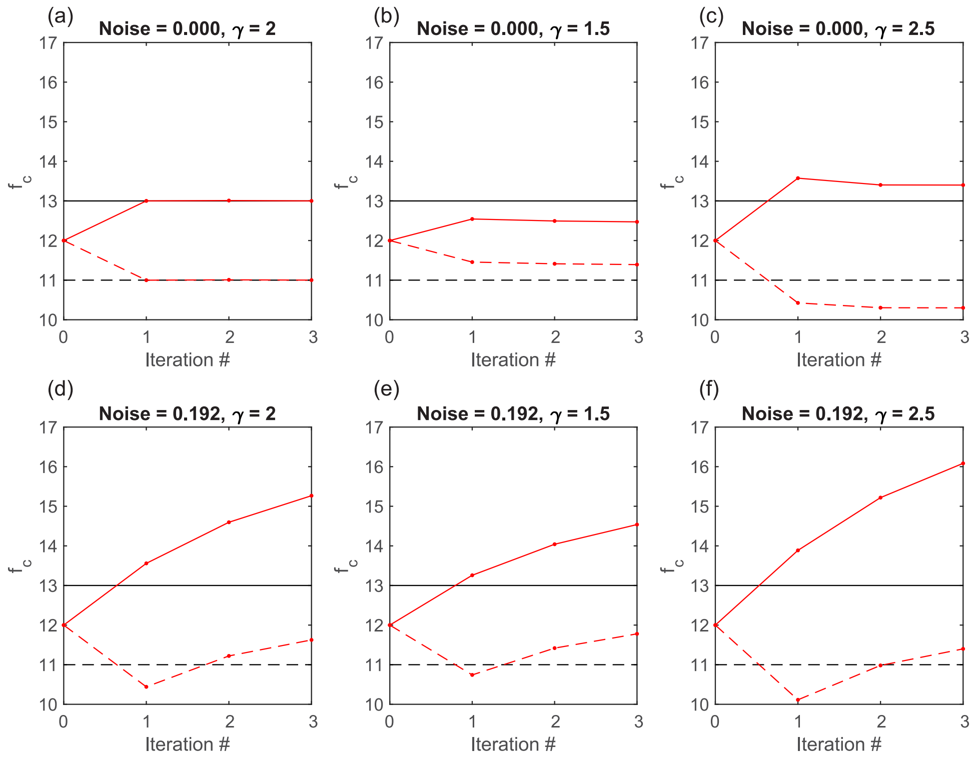

Figure 4. The evolution of inverted f_c with iterations for (a)–(c) noise-free and (d)–(f) noise-added synthetic tests that generated synthetic spectral ratio data with γ values of (a) and (d) 2, (b) and (e) 1.5 and (c) and (f) 2.5 and used a γ value of 2 for inversions. Black dashed and black solid lines represent the true f_c of events 1 and 2, respectively. Red dots connected by red solid and red dashed lines represent the inverted f_c for events 1 and 2, respectively, after each iteration except for the dots at iteration 0 that represent the initial f_c.

accurate spectral ratio dt^* data more heavily to further refine the structure in the source regions. As we will discuss in Section 5.2, however, for small-scale regions, such as The Geysers in this study, the spectral ratio dt^* data alone can well resolve both the overall and source-region structures, thus absolute t^* and single spectrum dt^* data are not required. We expect absolute t^* and single spectrum dt^* data would be helpful for the study of larger scale regions, for example, subduction zones.

3 SYNTHETIC TEST FOR EXTRACTING *dt** WITH THE SPECTRAL RATIO METHOD

We performed a series of synthetic tests to illustrate the effectiveness of our spectral ratio method and the code realizing the method. Effects of data noise and the assumed source spectrum model were considered. We simulated two events recorded by eight stations. The true f_c of the two events were set to be 11 and 13 Hz, which are typical corner frequencies for earthquakes at The Geysers based on our result in Section 4.2. The true differential t^* values at the eight stations range from -0.02 to 0.02, and the true Ω_0 ratios range from 1.0 to 4.5. We set different Ω_0 ratios at the different stations to represent the combined effects of differences in radiation pattern, geometric spreading, seismic moment and source-region density and velocity structures for the two events. The initial dt^* and Ω_0 ratio values were set 0.005 and 0.5 smaller than the true values, respectively, and the initial f_c values for both events were set to 12 Hz.

Fig. 1 shows the noise-free and noise-added synthetic spectral ratio data using the true, initial and inverted parameters. For noise-added tests, we constructed the noise for each station using the residuals between observed and predicted spectral ratios at eight actual stations after the inversion of real spectral ratio data for one representative event pair at The Geysers. The root-mean-square (rms) values of noise for all frequencies used at the eight stations are 0.179, 0.219, 0.157, 0.159, 0.271, 0.220, 0.205 and 0.079, as shown in Fig. 1(b). The noise added is moderate based on the analysis of spectral ratio residuals from real data inversions in Section 4.2. For noise-free tests, λ values are 0. For noise-added tests, we searched for λ values that yielded a condition number around 15. For all tests, we stopped the iterations when the rms residual reduction was smaller than 0.01.

Figs 2(a) and (d), 3(a) and (d), and 4(a) and (d) show the evolution of the inversion results with iterations for the noise-free and noise-added cases. For the noise-free test, all the parameters converged very quickly to their true values after three iterations (Figs 2a, 3a and 4a), and the modelled spectral ratio data from the inversion result perfectly fit the true data (Fig. 1a). For the noise-added test, although the convergence of f_c was not stable, all dt^* and most Ω_0 ratios were slightly biased but still converged to close to their true values except for the Ω_0 ratio at one station, which failed to converge and was accompanied by relatively poor recovery of dt^* (Figs 2d, 3d and 4d).

One possible source of error in the solutions using our method is caused by assuming a Brune (1970) source model ($\gamma = 2$). To test the effect of using the Brune model when the real source spectrum model is different, we synthesized noise-free and noise-added data using γ values of 1.5 and 2.5 and then performed inversions assuming γ to be 2. The results of these tests are shown in

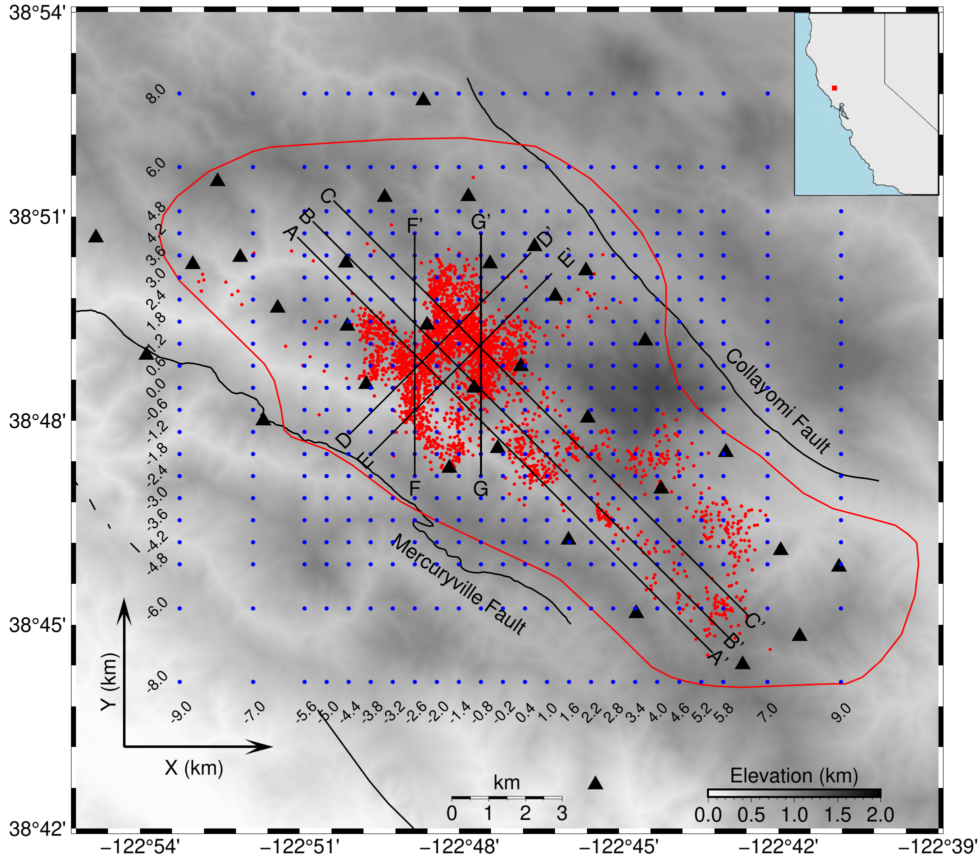

Figure 5. Map view of earthquakes (red dots) and stations (triangles) at The Geysers geothermal field, outlined by the red curve, and the coordinate system used for velocity and attenuation tomographic inversions. Blue dots represent the grid nodes in X (longitude) and Y (latitude) directions, the coordinates of which are labelled. Mercuryville and Collayomi Faults are shown as black lines. Lines AA′–GG′ denote the model cross-sections shown in Fig. 10. The background image shows the topography. The upper right inset shows the geographic location of The Geysers, which is indicated by a red square.

Figs 2–4. With noise-free data, it can be seen that using an inaccurate γ affects the accuracy of the final Ω_0 ratio and f_c solutions but has only a slight effect on dt^* solutions (Figs 2b and c, 3b and c, 4b and c). For noise-added data, the errors in the final solutions due to the inaccurate γ fall within the errors due to data noise (Figs 2e and f, 3e and f, 4e and f). However, the small effect of inaccurate γ on the recovery of dt^* may be because the two events have similar f_c values in these synthetic tests. Eq. (4) shows that, if two events have exactly the same f_c, their spectral ratios at all stations have no sensitivity to the error in source model (γ). To assess whether more different f_c values for the two events can result in a larger effect of an inaccurate source model on the inversion of dt^*, we performed several additional tests, which are similar to the tests described above except setting the true f_c values to be 8 and 16. Compared to the results shown in Fig. 2, the results from the new tests (Fig. S1, Supporting Information) only show slightly worse recovery of dt^* due to the inaccurate source models, especially for the noise-added tests. These tests indicate that the inversion of dt^* using our spectral ratio method is not significantly affected by the choice of a particular source model.

4 APPLICATION TO THE GEYSERS GEOTHERMAL FIELD, CALIFORNIA

We used 2994 earthquakes recorded by a 34-station seismic network at The Geysers from 2011 (Fig. 5). These events were selected because they can be paired with closely located earthquakes in 2005, in preparation for a future tomographic study of the change in Q between 2005 and 2011. Here we focus on the application and validation of the new DDQ tomography method. The following sections cover (1) the inversion for earthquake relocations and a new Vp model, (2) extracting absolute t^* and event-pair dt^* data, (3) quality control of the dt^* data and (4) DDQ tomographic inversions with synthetic and real data.

4.1 DD earthquake relocation and *Vp* tomography

For Q tomography, earthquake locations and a velocity model are required in advance. We began by repicking P-wave first arrivals in the waveform time windows around catalogue picks using an automatic seismic arrival picking code (Guo *et al.* 2018b), which is based on the Akaike Information Criteria method (Maeda 1985). We also calculated P- and S-wave waveform cross-correlation (WCC) differential times from pairs of nearby events separated by less than 2 km on common stations. Similar to Lin (2015), we required each event pair to have an average WCC coefficient larger than 0.5 and at least eight individual differential times with WCC coefficient larger than 0.7. With the repicked P-wave arrival times and P-wave WCC differential times, we performed a DD tomographic inversion for new earthquake locations and a new Vp model starting from catalogue earthquake locations (Gritto & Jarpe 2014) and a previous Vp model at The Geysers (Gritto *et al.* 2013). Note that the DD tomography was performed with the new tomoTD code instead of the original tomoDD code, so the station correction terms were

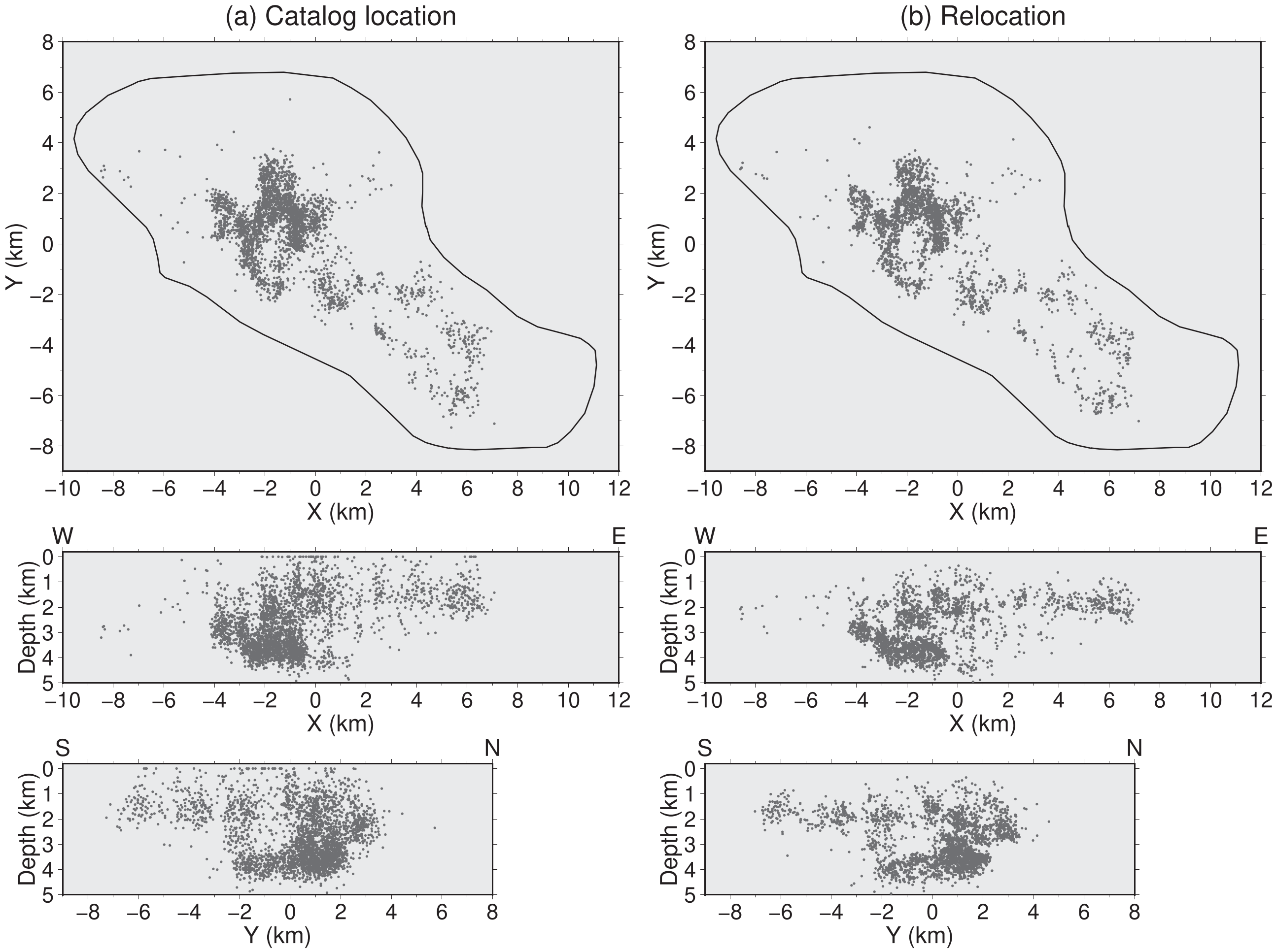

Figure 6. Comparison of (a) catalogue earthquake locations and (b) our earthquake relocations in this study in map view, EW cross-section and NS cross-section. The Geysers geothermal field is outlined by the black curve.

included in the inversion. This can reduce the effect of unmodelled velocity structure at shallow depths on the earthquake locations and velocity model at greater depth. The node spacings of the coordinate system in the X (longitude), Y (latitude) and depth directions were set to 0.6, 0.6 and 0.4 km, respectively, in the geothermal area (Fig. 5).

We modified the standard way of constructing catalogue differential arrival time data from absolute arrival time data used for DD tomography, which is through a code ph2dt provided with the DD location code hypoDD (Waldhauser 2001). ph2dt constructs event pairs by searching for a specified number of nearby events for each event. This can result in small inter-event distances for events in zones with concentrated earthquakes and large inter-event distances in zones with sparsely distributed earthquakes. This is well designed for determining high-precision relative locations, for which the inter-event distance is a key factor (Waldhauser & Ellsworth 2000). However, this is not suitable for the imaging of concentrated earthquake zones because the constructed differential data there, with inter-event distances potentially much shorter than the size of the grid spacing, would have small sensitivities to velocity parameters, resulting in low model resolution of these zones. More generally, the distribution of inter-event distances for event pairs constructed in this way in the whole study region is non-uniform, which would result in non-uniform model sensitivities of differential data in different parts of the study region.

To address these problems, we developed a new 'best cell event' method that constructs catalogue differential data with the following steps:

(1) We generated all possible catalogue differential data from catalogue absolute data for all the event pairs with inter-event distance less than a threshold.

(2) We meshed the whole volume uniformly with grid intervals in three directions being the minimum size that is expected to be resolved, which is generally the same as that used for the tomographic inversion.

(3) Each cell was further divided into eight uniform subcells with dimensions of half of the grid intervals. In each subcell, we identified up to three events with the most differential data and used the one with highest average weight of the associated differential data among them as the subcell event.

(4) Finally, the differential data for pairs of subcell events were selected and used for the subsequent tomographic inversion.

Before constructing catalogue differential data using the new method, we made a preliminary joint inversion of earthquake locations and velocity model with ph2dt-derived differential data and used the relocations as the input for this procedure, so that the determination of subcell events could be more accurate. In addition to constructing catalogue differential data, the above steps 2–4 were

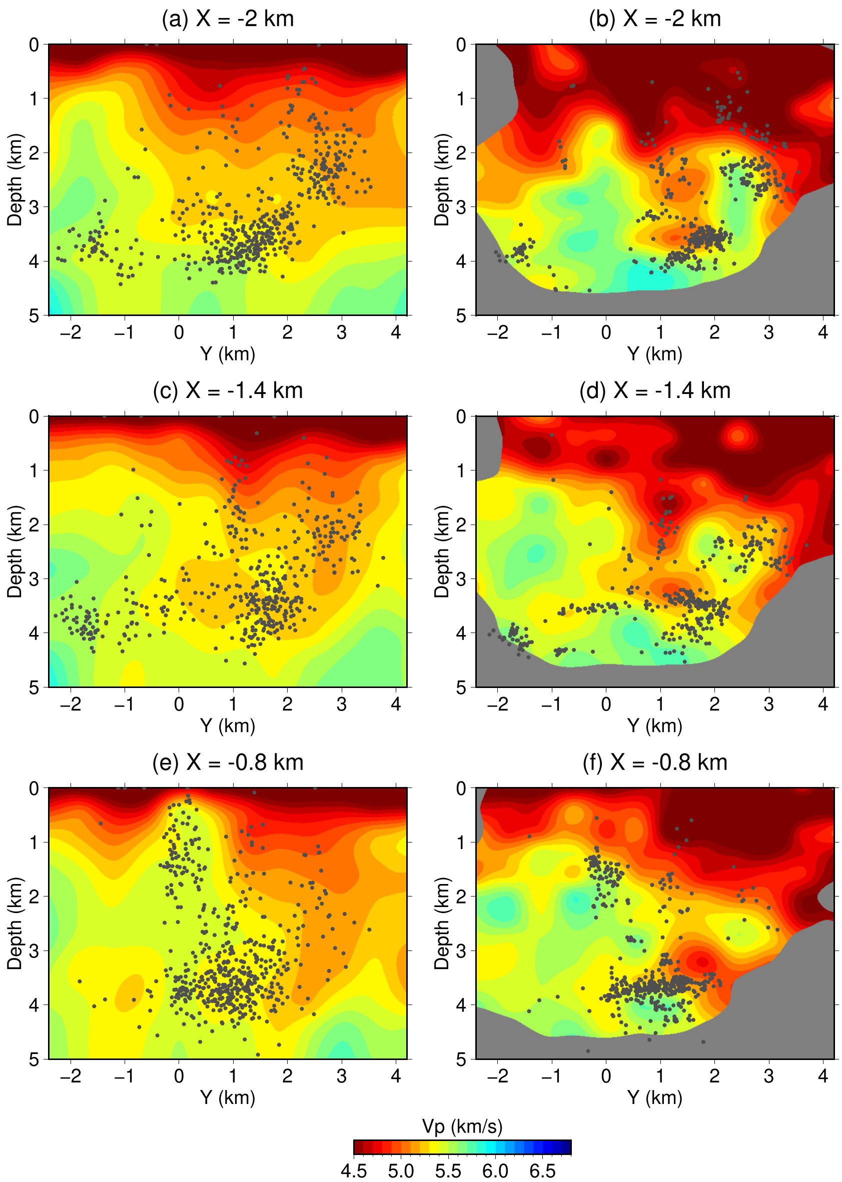

Figure 7. The comparison of (a), (c) and (e) catalogue earthquake locations and the Vp model from Gritto *et al.* (2013) and (b), (d) and (f) our earthquake relocations and our new Vp model along cross-sections at $X = -2$, -1.4 and -0.8 km. Earthquakes within 0.3 km of each cross-section are shown. For the cross-sections of the new Vp model, the low-resolution regions estimated from the checkerboard resolution test shown in Fig. S3 in the Supporting Information are masked.

also used to process the WCC differential data. Finally, we obtained 6222 632 catalogue differential times for 1238 subcell events and 361 752 WCC differential times for 1212 subcell events, which are used for the final DD tomography along with the 74 652 absolute times for 2937 events. The damping and smoothing parameters used for tomography were selected based on a joint analysis of the trade-off curve between misfit and model norm (Fig. S2, Supporting Information) and the condition number of the inversion system. Since the new best cell event method is designed for velocity model tomography but is not ideal for constraining relative locations of closely located earthquakes, we further relocated all the earthquakes with the new Vp model using the ph2dt-derived catalogue differential times and all WCC differential times.

After the inversion, we determined new locations for 2934 earthquakes. Fig. 6 shows a comparison of the initial catalogue locations and our earthquake relocations. Our relocations are much more concentrated, suggesting improved relative locations among events. Fig. 7 shows a comparison of the previous and our new Vp models along several north–south cross-sections. We performed a checkerboard test to estimate the resolution of our new model. We first created the true checkerboard model that has 5 per cent positive and negative anomalies relative to the starting model applied to nodes in a 2-by-2-by-2 pattern (Fig. S3, Supporting Information). We then generated noise-free synthetic data with the true checkerboard model and performed an inversion with the synthetic data using the same inversion parameters and starting model as the real data inversion. Fig. S3 in the Supporting Information shows the recovered checkerboard model along the same cross-sections shown in Fig. 7, which shows that the earthquake generation zones are well resolved. Compared to the previous model, our new Vp model shows finer-scale structures at depth, in particular low-Vp anomalies that are spatially correlated with earthquake locations (Fig. 7). Our

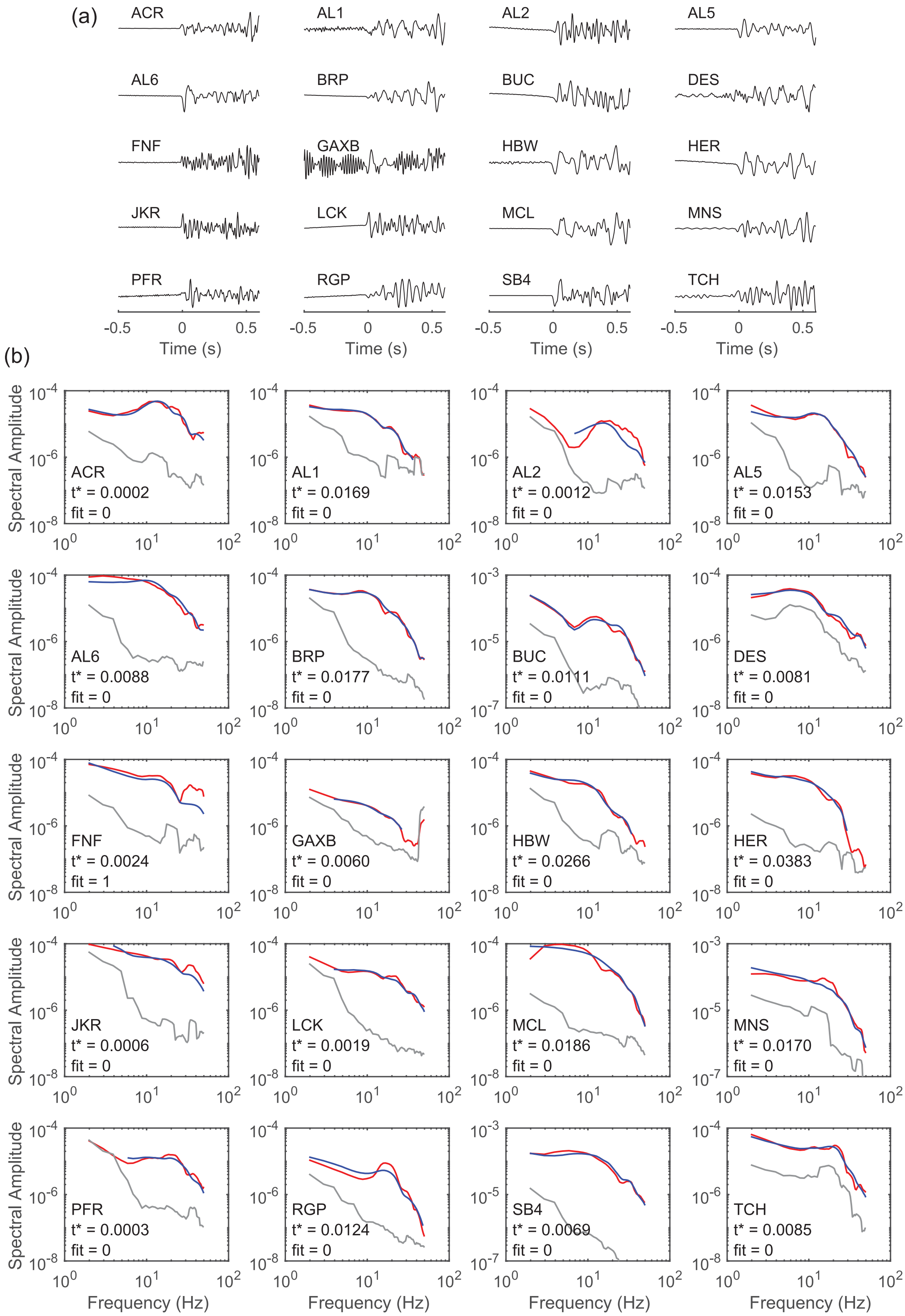

Figure 8. Single spectrum inversion result for one example event. (a) Normalized velocity seismograms of the example event on the vertical component at 20 stations as labelled on the left of each subplot. (b) Fitting of displacement spectra at each station using the single spectrum method for the example event. Red and grey lines are observed signal and noise spectra, respectively. Blue lines are the modelled signal spectra within usable frequency ranges using solutions from single spectrum inversion. For this event, its magnitude is 1.7, its depth is 3.59 km, its f_c value from the single spectrum inversion is 12.4 Hz, and its inverted t^* and fit quality at each station are as indicated.

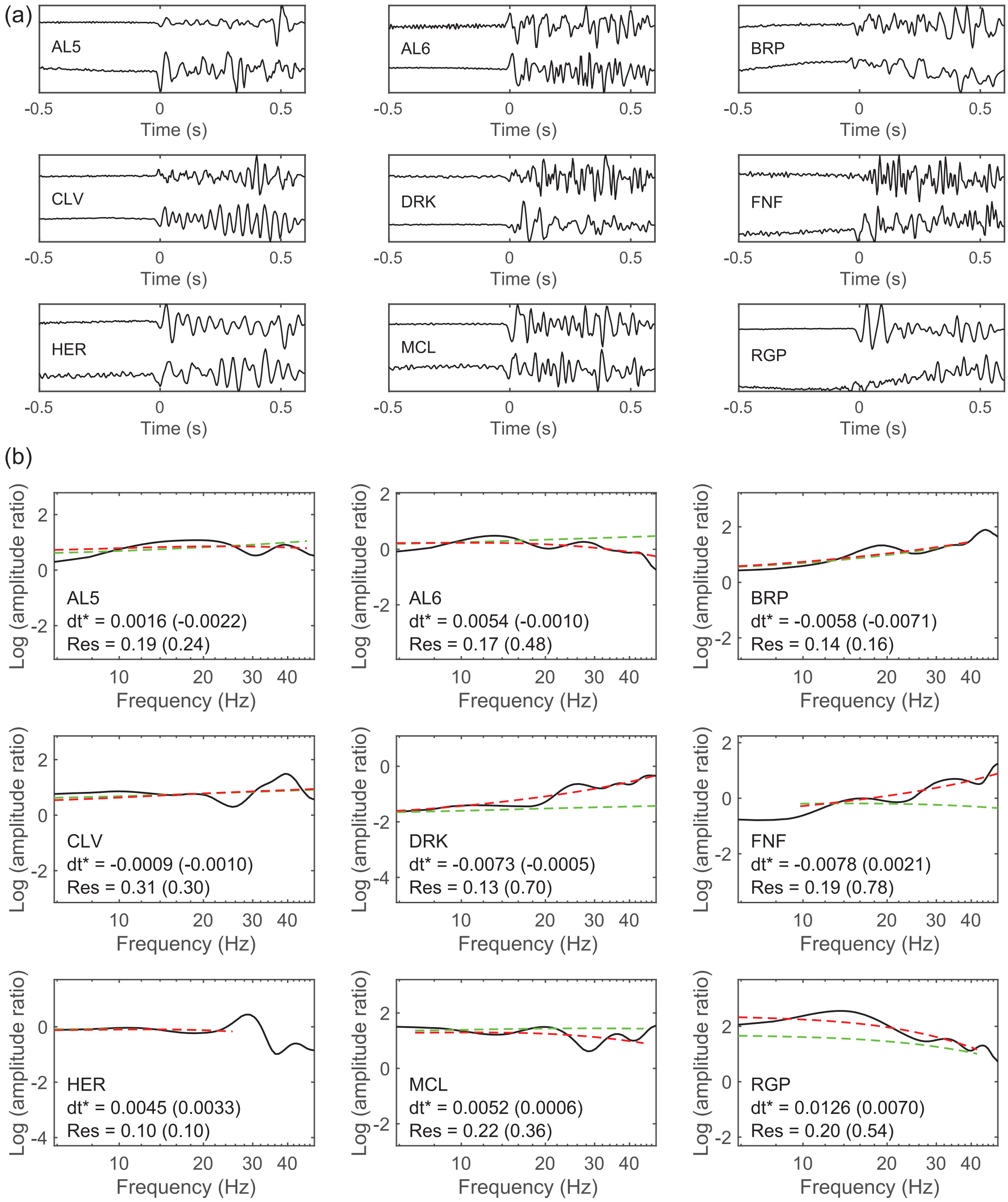

Figure 9. Spectral ratio inversion result for one example event pair. (a) Normalized velocity seismograms of the two example events on the vertical component at nine stations as labelled on the left of each subplot. In each panel, the top and bottom seismograms correspond to the first and second events, respectively. (b) Observed and modelled spectral ratio data in natural logarithm domain as a function of frequency at each station. Solid black lines represent the observed spectral ratios. Green and red lines represent the modelled spectral ratios within usable frequency ranges using solutions from spectral ratio inversion and single spectrum inversion, respectively. Note that the single spectrum inversion solutions are the initial parameters of the spectral ratio inversion. The inverted dt^* and final data residual at each station from the spectral ratio inversion are shown on the bottom left, followed by the corresponding single spectrum results in parentheses. For these two events, their magnitudes are 1.3 and 1.0, their depths are 3.61 and 3.02 km, the distance between them is 2.15 km, and their f_c values from the spectral ratio inversion are 12.8 and 10.6 Hz.

earthquake relocations and new *Vp* model are discussed in more detail in Section 5.3.

4.2 Extracting spectral ratio dt^*

In this section, we first describe the details of single spectrum and spectral ratio inversions and then discuss how we select high-quality spectral ratio dt^* data.

Good initial parameters can facilitate convergence to the correct solution for the nonlinear problem of spectral ratio inversion. Here, we used a method that could simultaneously determine Ω_0, f_c, t^* and site response by jointly inverting spectra for a large set of earthquakes and stations (Pesicek *et al.* 2011; Bisrat *et al.* 2014; Ohlendorf *et al.* 2014) to obtain initial parameter values for the spectral ratio inversion. The details of this single spectrum method can be found in Bisrat *et al.* (2014). Similar to Bisrat *et al.* (2014),

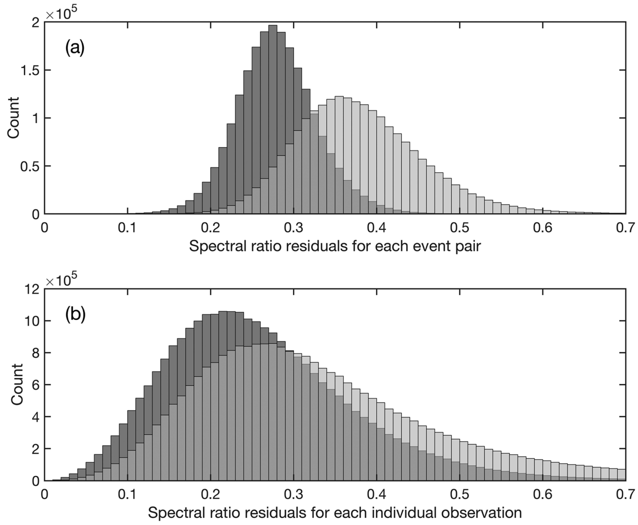

Figure 10. Histograms of initial (light grey) and final (dark grey) spectral ratio residuals (a) for each event pair and (b) for each individual observation.

a series of criteria were designed to process the raw waveform data and select the ones that can be used for the single spectrum inversion and the subsequent spectral ratio inversion. All vertical component waveforms were first processed by removing the mean and linear trend. We then calculated signal spectra from 1.024 s time windows around *P*-wave arrivals (0.424 s before the arrival and 0.6 s after the arrival) and noise spectra from 1.024 s time windows before the signal windows using a multitaper spectrum estimation method (Thomson 1982) with a frequency range of 1.67–50 Hz. To avoid contamination of *P*-wave signals by *S*-wave signals, only waveforms with an *S*–*P* arrival time difference above 0.7 s were used. The calculated spectra were then smoothed with a 3-point-long moving window. SNRs were then calculated for all spectra. The signal spectra were selected for the single spectrum inversion if the SNR was above a threshold of 2.5 in a continuous frequency range of at least 10 Hz. After the single spectrum inversion, the obtained t^* solutions were assigned quality values 0 (best) to 4 (worst) based on the fit between the observed and predicted spectra. After the single spectrum inversion with data from 2962 events, we obtained 54 611 t^* values of quality of 0, 1 and 2, which were used as the initial parameters for the subsequent spectral ratio inversion. The single spectrum inversion result for one example event is shown in Fig. 8.

For the spectral ratio inversion, the data pre-processing steps are the same as that used for the single spectrum inversion. After obtaining the individual spectra and the corresponding SNRs, we calculated spectral ratios for each event pair with an inter-event distance less than 3 km if the SNRs of both spectra were above 3 within a common and continuous frequency range of at least 10 Hz. The calculated spectral ratios were smoothed with a 5-point-long moving window and then used for the spectral ratio inversion. After the inversion using a frequency range of 1.67–50 Hz, we found that, overall, the frequency range below ∼5 Hz had larger misfit than higher frequencies, therefore we modified the frequency range to 5–50 Hz for the final inversion. For the damping parameter λ, we searched for a value that could constrain the condition number of the inversion system to be ∼10. Overall, the resulting resolution values of all parameters for all spectral ratio inversions using the selected λ values are around 0.5. We stopped the iterations when the rms spectral ratio misfit did not change significantly or reached the predetermined maximum number of iterations (20). Overall, most inversions converged very quickly after 1–3 iterations.

We obtained 27 333 915 dt^* measurements for 2196 869 event pairs with inter-event distances less than 3 km. On average, each event pair has ∼12 dt^* measurements. Fig. 9 and Fig. S4 in the Supporting Information shows the fitting of spectral ratios with initial parameters, that is, the single spectrum method result, and the spectral ratio method result for one and two example event pairs, respectively. Fig. 10 shows the comparison of initial and final spectral ratio residuals for each event pair and for each station for each event pair. The mean reduction in spectral ratio residual for each event pair is ∼25 per cent. The mean reduction in spectral ratio residual for each station for each event pair is ∼20 per cent. The reduction in spectral ratio residuals indicates improved quality of the spectral ratio method result compared to the single spectrum method result.

In addition to dt^*, our spectral ratio inversions also provide f_c estimates. For each event pair with multiple nearby events, there are multiple f_c estimates, which are varied due to measurement errors. Fig. S5(a) in the Supporting Information shows all the f_c estimates for one example event. The mean and standard deviation of all the f_c estimates for each event can be calculated and used as the final f_c value and the uncertainty of the final f_c for the event. Fig. S5(b) in the Supporting Information shows the histogram of final f_c values for all events. Fig. S6(a) in the Supporting Information shows the relation between f_c and seismic moment for all events, which is consistent with the scaling relation determined by Johnson (2014). Fig. S6 in the Supporting Information also shows that the earthquakes we used at all depths have stress drops of ∼0.1–20 MPa, and most of them have small stress drops of ∼0.1–1 MPa. The earthquakes with small stress drops may be correlated with regions with injected fluids. Similar results are also observed by Yu *et al.* (2020). They used a spectral ratio method to estimate source parameters of co-located induced earthquakes in northeast British Columbia, Canada, and found that earthquakes proximal to a hydraulic fracturing well have an order of magnitude smaller stress drop (∼0.1–1 MPa) than the earthquakes distal to the well (∼1–10 MPa). Although the spatial distribution of earthquake stress drops may be of interest in terms of understanding how fluid injection and steam production change the reservoir conditions, a detailed analysis requires precise estimates of seismic moments and is beyond the scope of this paper.

4.3 Quality control

After obtaining the *P*-wave spectral ratio dt^* data for all the event pairs used, we applied a set of criteria for quality control on the data.

(1) We required that, for both events of all event pairs, their f_c estimates need to be within 1.96 times the standard deviation from their final f_c values. The dt^* data of the event pairs that do not fit this requirement were removed.

(2) We placed two requirements on the spectral ratio residual, one on the overall rms residual for each event pair and one on the rms residual of each station for each event pair. If the overall rms residual for one event pair is high, all the solutions for that event pair may be of low quality even though some stations may have small residuals. Thus, we required the rms residual of each event pair to fall below a threshold (0.35), which is called the event-pair residual threshold. We further required the residual for each station of each event pair to fall below a threshold (0.3), which is called the individual residual threshold.

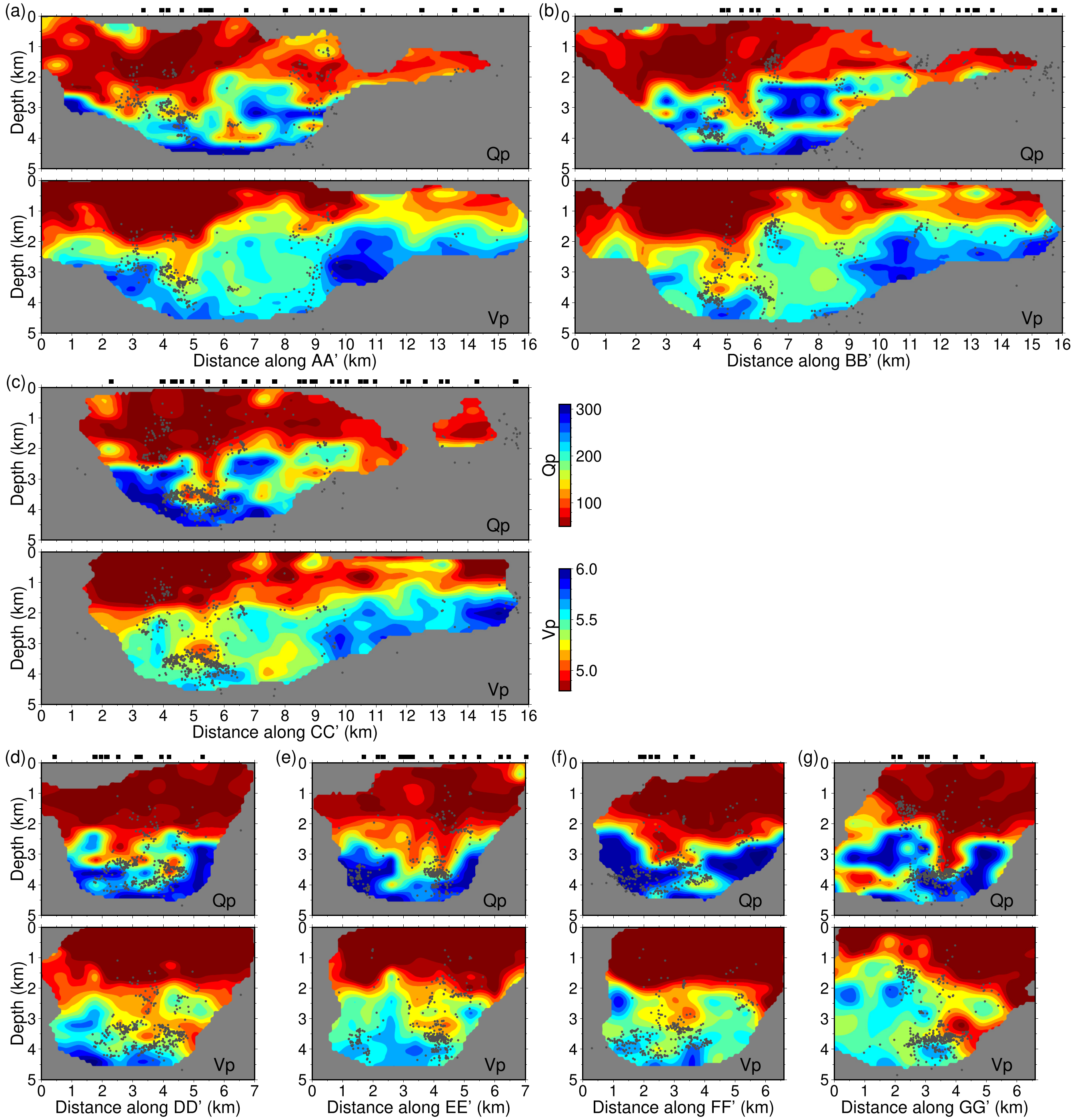

Figure 11. Cross-sections of the final Qp and Vp models along profiles AA′–GG′ shown in Fig. 5. Earthquakes (dots) within 0.3 km of each cross-section are shown. Black squares represent surface locations of the active wells within 0.3 km of each cross-section, which are obtained from the California Geologic Energy Management Division (https://www.conservation.ca.gov/calgem/). Low-resolution regions estimated from the noise-free checkerboard test are masked.

(3) Since the attenuation parameter is more sensitive to the amplitude decay of the high-frequency part of the spectrum, the usable frequency range for each station of each event pair was required to have a width of at least 10 Hz above the final f_c values of both events.

(4) Another useful way to estimate dt^* quality is to calculate closure error. Let dt^*_{12}, dt^*_{13} and dt^*_{23} represent the dt^* data of three event pairs on a common station and then let $ddt = dt^*_{12} - dt^*_{13} + dt^*_{23}$. We define ddt as closure error, which should be 0 if there is no error in each dt^*. After calculating all the closure errors that are linked with dt^*_{12}, we can use the average of their absolute values to evaluate the error of dt^*_{12}. Fig. S7 in the Supporting Information shows the histogram of closure errors for all selected data after the application of the criteria in steps (a)–(c). We then required the closure error of each dt^* to fall below a threshold (0.0025). We find that there is a roughly linear trend between the closure error and individual residual for the dt^* data, suggesting that both of them mainly result from a common source of error, which is likely to be the dt^* data error.

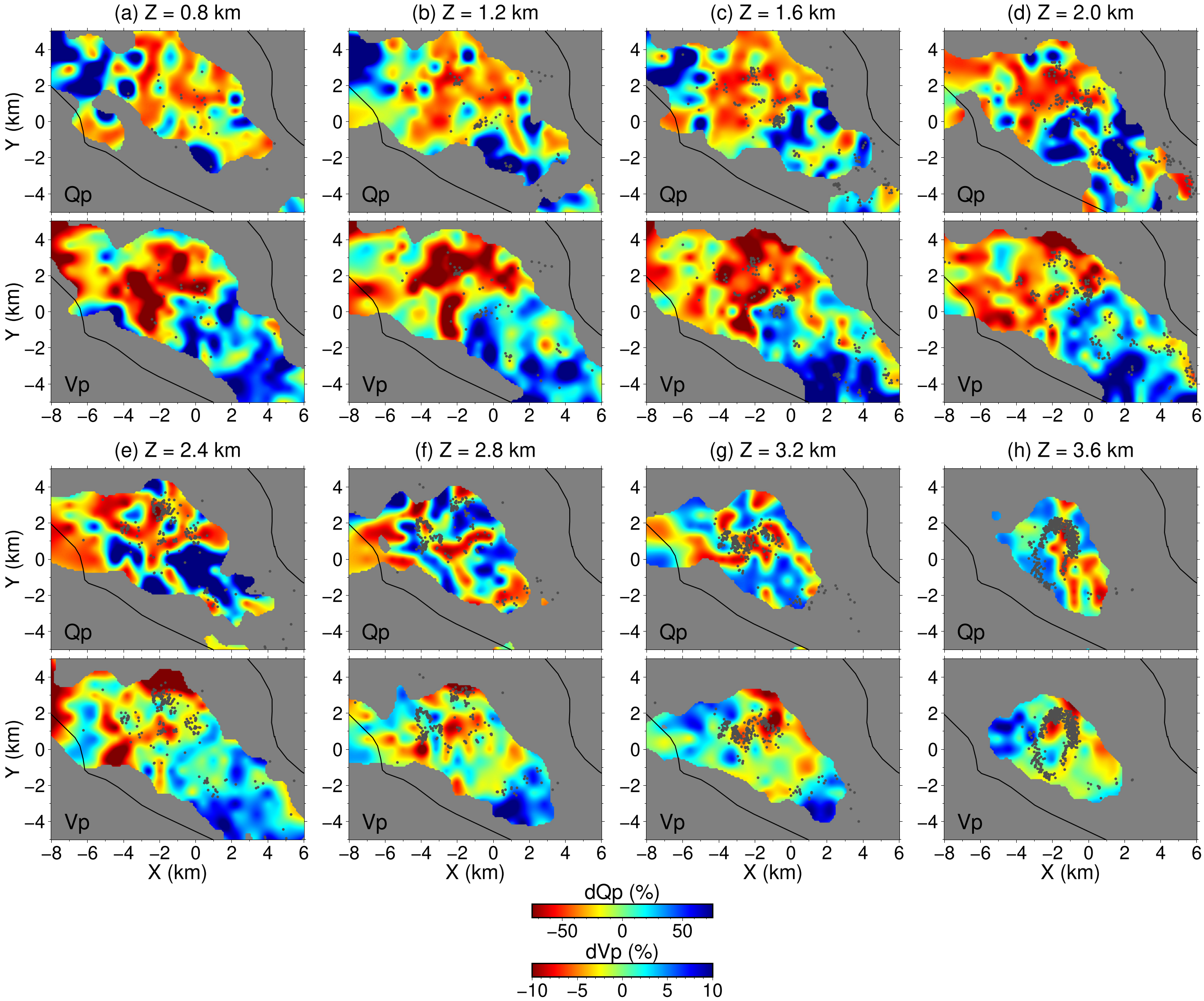

Figure 12. Map views of final Qp and Vp model perturbations from mean values at depths of 0.8–3.6 km in 0.4 km intervals. Earthquakes (dots) within 0.2 km of each slice are shown. Black lines represent boundaries of the geothermal field as shown in Fig. 5. Low-resolution regions estimated from the noise-free checkerboard test are masked.

Applying the above criteria on f_c, event-pair residual, individual residual, high-frequency bandwidth and closure error in sequence removed 2400 058 (8.8 per cent), 1750 701 (6.4 per cent), 6612 768 (24.2 per cent), 1509 497 (5.5 per cent) and 884 031 (3.2 per cent) spectral ratio dt^* data, respectively, leaving 1867 903 (85.0 per cent) event pairs and 14 176 860 (51.9 per cent) spectral ratio dt^* data.

4.4 DDQ tomographic inversion and model resolution tests

Steps 2–4 of the new best cell event method used to select differential arrival time data for DD velocity tomography described in Section 4.1 were also used to process the spectral ratio dt^* data. In the end, we were left with 1569 578 P-wave spectral ratio dt^* data from 1133 earthquakes, which were used for the DDQ tomography. We performed a preliminary DDQ tomographic inversion starting with a homogeneous model with a constant Qp value of 150 and used the average values of the inverted Qp model at each depth as the starting 1-D model for the final DDQ tomographic inversion. During the inversion, we gradually decreased the maximum inter-event distance for the dt^* data from 3 to 2 to 1 km as iterations progressed to gradually refine the source-region structure. The smoothing and damping values were selected based on a joint analysis of the trade-off curve between misfit and model norm, the condition number of the inversion system, and checkerboard tests. After the inversion, the rms residual of dt^* data decreased from 0.009 to 0.007. Figs 11 and 12 show cross-sections and depth slices of the inverted Qp model, respectively, along with our new Vp model. To compare the new DDQ tomography method with the standard Q tomography method using absolute t^* data, we also performed the inversion using absolute t^* data only (Fig. 13a). 52 565 absolute P-wave t^* data with quality of 0 and 1 from 2906 relocated earthquakes were used. Discussion of the comparison is given in Section 5.1.

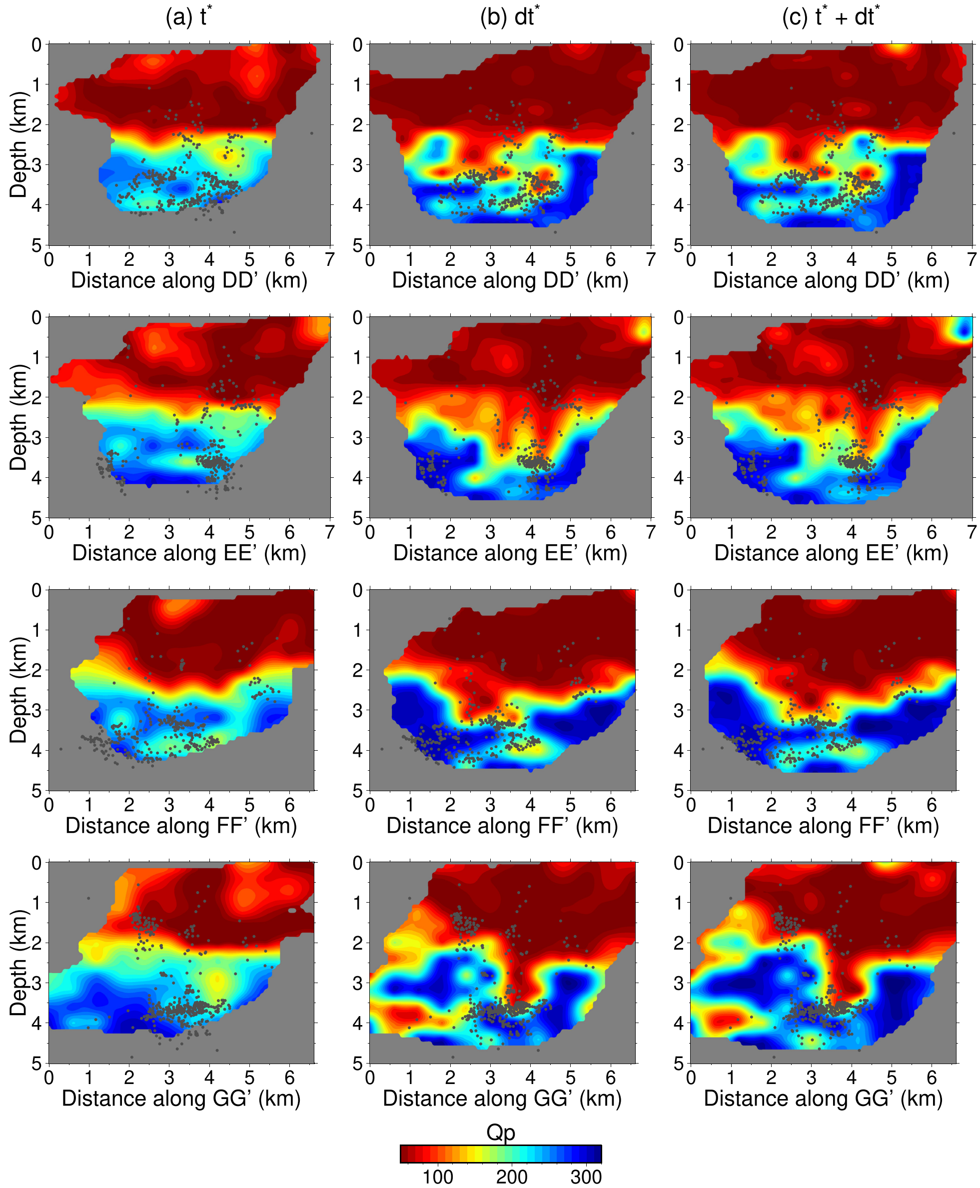

Figure 13. Cross-sections of the inverted Qp models along profiles DD′, EE′, FF′ and GG′ using (a) absolute t^* data only, (b) spectral ratio dt^* data only and (c) absolute t^* and spectral ratio dt^* data. Low-resolution regions estimated from the noise-free checkerboard test are masked.

To estimate the resolution of the inverted Qp models, we performed synthetic resolution tests, including checkerboard tests and restoration tests with and without noise. For the checkerboard test, the input true model has 50 per cent positive and negative anomalies applied to nodes in a 2-by-2-by-2 pattern relative to the starting model. For the restoration test, the input true model was the model from the DDQ tomographic inversion. For the noise-added tests, we added Gaussian random noise with zero mean and a standard deviation of 0.006 for both the synthetic t^* and dt^* data. All the inversion strategies and parameters for all the tests were the same as the ones used for the real data inversions. These resolution tests show that, for the DDQ model, the regions where earthquakes occur are well resolved (Figs 14–17). We also calculated checkerboard model resolvability at each node for each checkerboard model (Figs 14 and 15) based on the method of Zelt (1998). The regions with checkerboard model resolvability values larger than 0.7 are well recovered (Figs 14 and 15). Interpretation of the results is given in Section 5.3.

5 DISCUSSION

5.1 Comparison of the standard Q and DDQ tomography methods

For the Qp models from DDQ tomography using spectral ratio dt^* data and standard Q tomography using absolute t^* data, there are differences between them at all depths (Figs 13a and b). In particular, at depths greater than ∼2 km where earthquakes are concentrated, the Qp model from DDQ tomography shows high attenuation anomalies that are spatially correlated with earthquakes (Fig. 13b). These anomalies are not present in the Qp model from

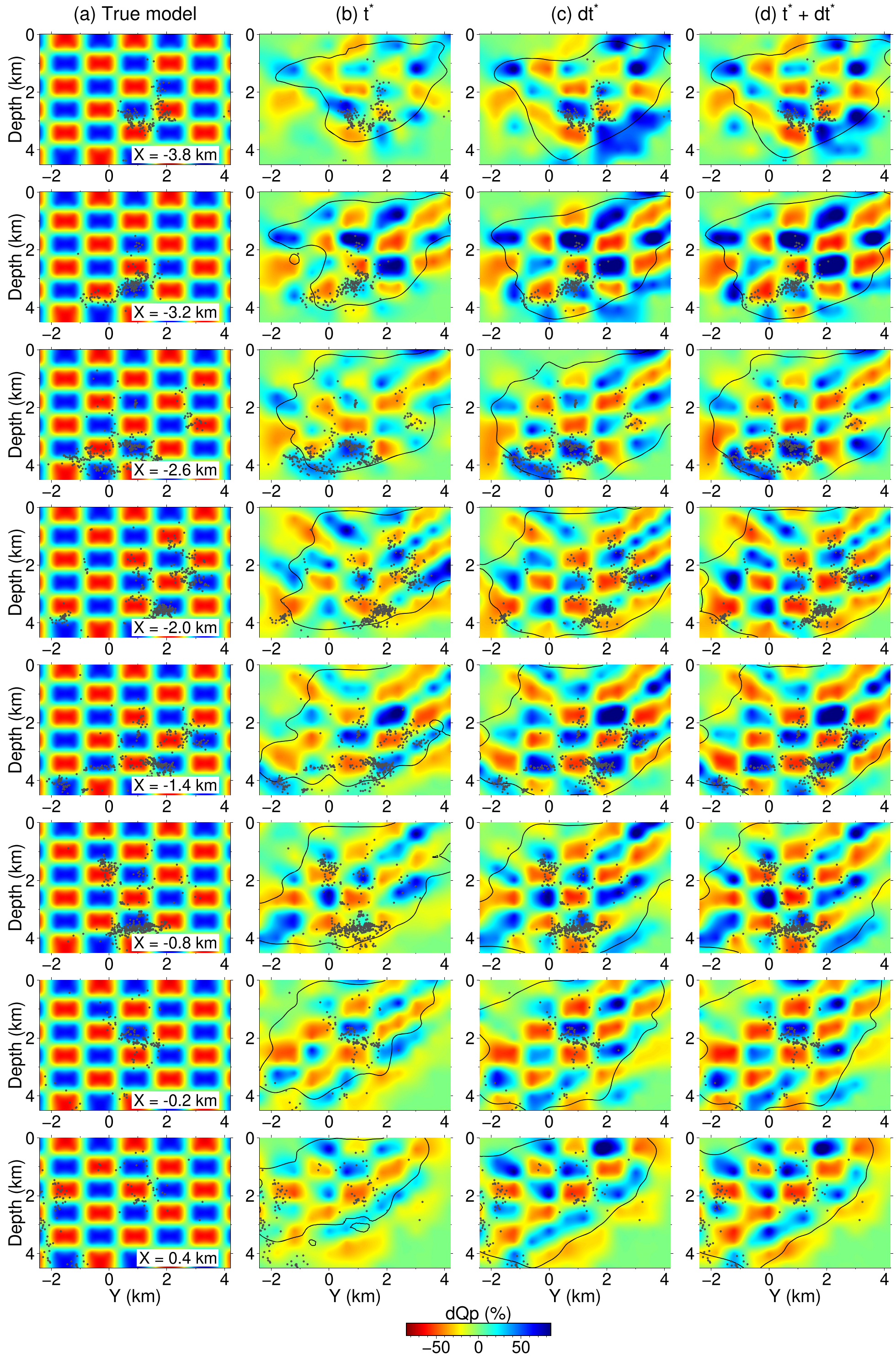

Figure 14. Cross-sections of the (a) input true and (b)–(d) inverted Qp models from noise-free checkerboard tests using (b) absolute t^* data only, (c) dt^* data only and (d) absolute t^* and dt^* data. Black curves represent the contour of checkerboard model resolvability of 0.7. Dots represent earthquakes within 0.3 km of each cross-section.

standard Q tomography (Fig. 13a). Both the noise-free (Figs 14b and c and 16b and c) and noise-added (Figs 15b and c and 17b and c) checkerboard and restoration tests show that the dt^* inversion can better recover the true model than the t^* inversion, especially in earthquake source regions. These results clearly indicate that the new DDQ tomography method using spectral ratio dt^* data can determine higher resolution attenuation structure than the standard method using t^* data.

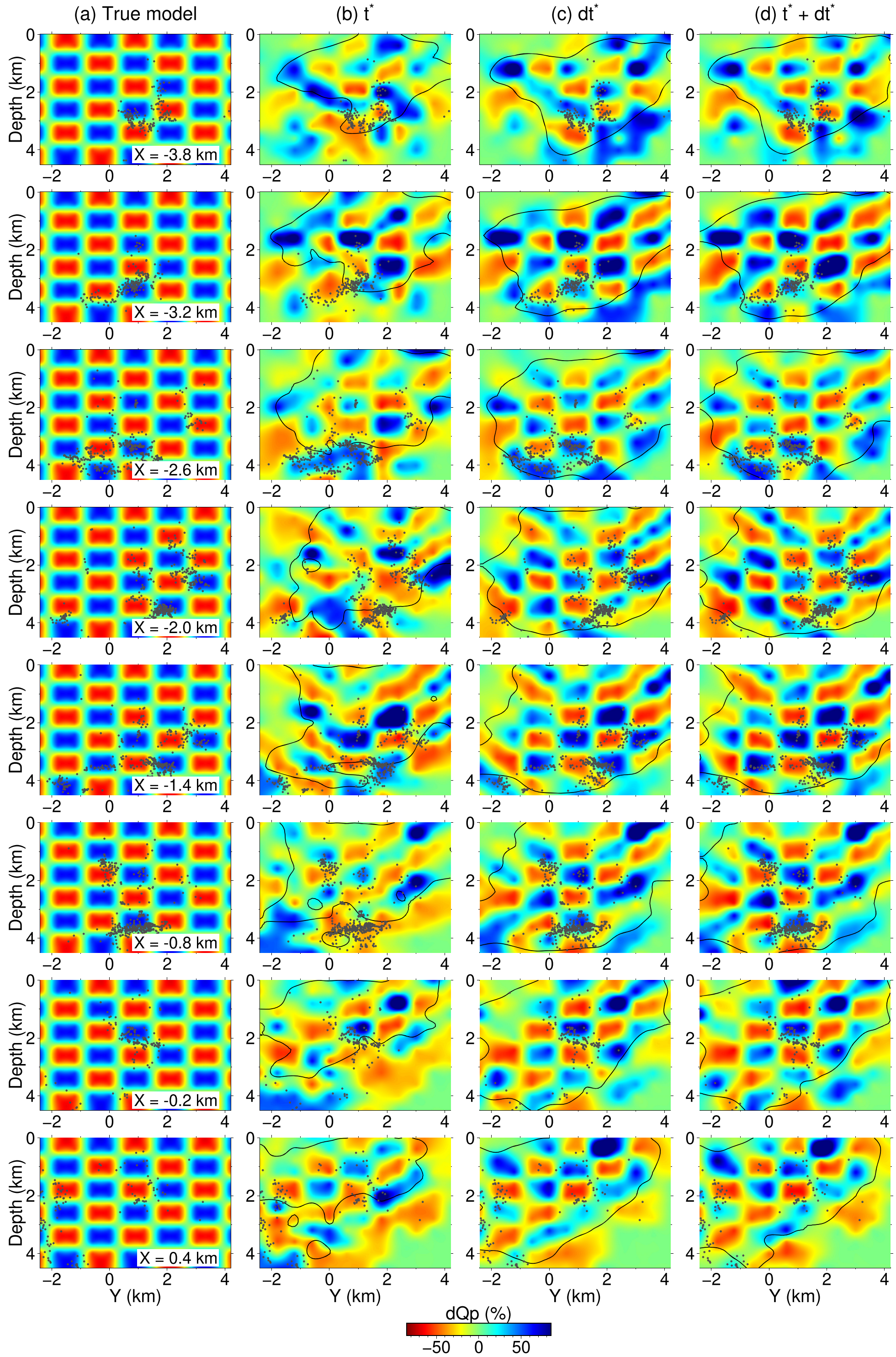

Figure 15. Cross-sections of the (a) input true and (b)–(d) inverted Qp models from noise-added checkerboard resolution tests using (b) absolute t^* data only, (c) dt^* data only and (d) absolute t^* and dt^* data. Black curves represent the contour of checkerboard model resolvability of 0.7. Dots represent earthquakes within 0.3 km of each cross-section.

5.2 Importance of inter-event distance on DDQ tomography

For the DD location method, Waldhauser & Ellsworth (2000) proposed to use catalogue differential time data constructed from absolute time data along with the more accurate WCC differential time data with a hierarchical weighting strategy. For the DD velocity tomography method, Zhang & Thurber (2003) adopted a similar strategy that jointly uses catalogue absolute, catalogue differential and WCC differential time data. The idea is that the absolute data can better constrain absolute earthquake locations and large-scale structure, catalogue differential data can better constrain relative earthquake locations and source-region structure, and more

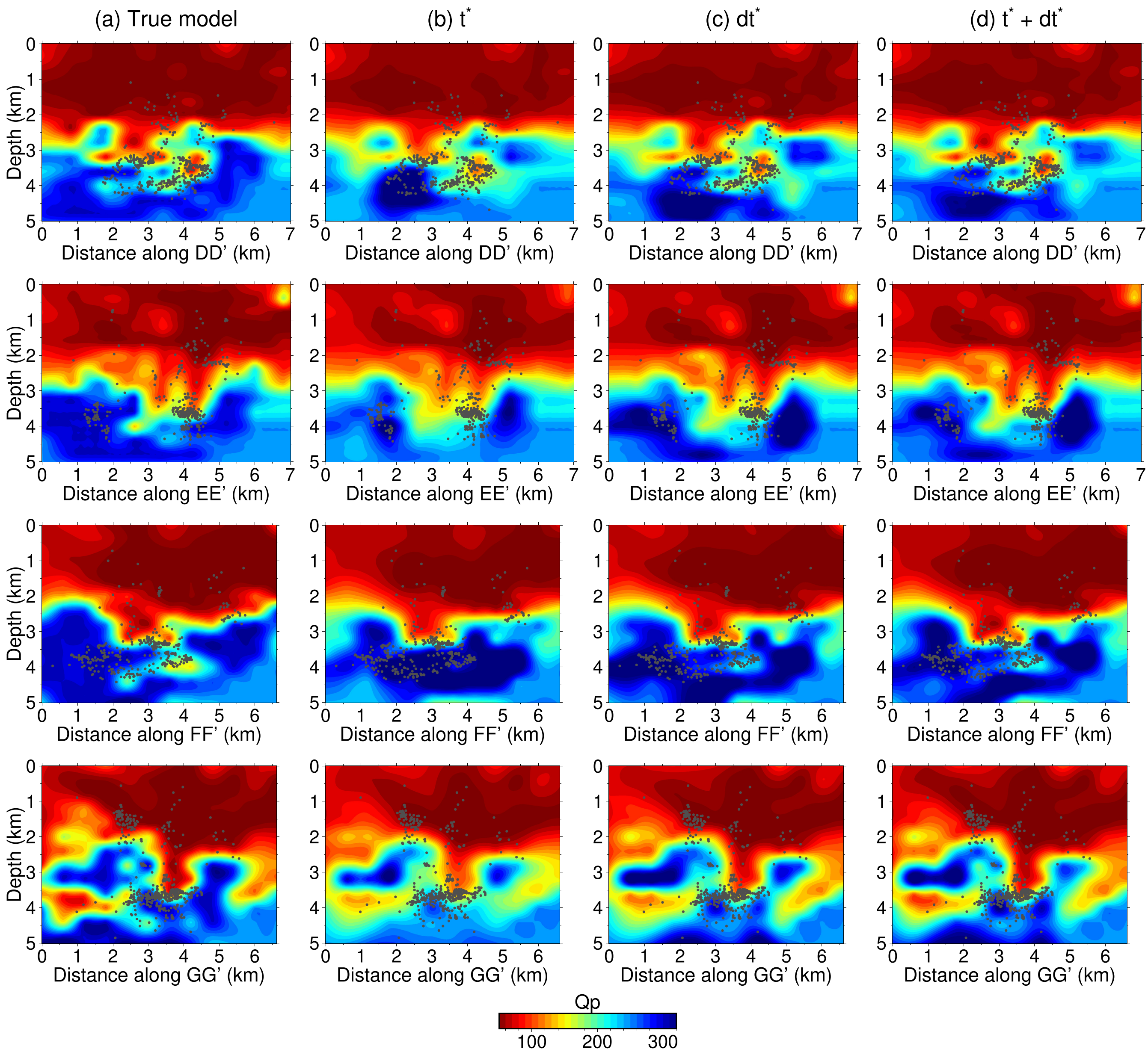

Figure 16. Cross-sections (DD′, EE′, FF′ and GG′) of the (a) input true and (b)–(d) inverted *Qp* models from noise-free restoration tests using (b) absolute t^* data only, (c) dt^* data only and (d) absolute t^* and dt^* data. Dots represent earthquakes within 0.3 km of each cross-section.

accurate WCC differential data, if available, can further constrain relative earthquake locations and source-region structure. For the DD location and tomography methods, the reason to use such a strategy rather than using the more accurate WCC differential data only is that measuring WCC differential data is greatly limited by inter-event separation as shown in many studies (e.g. Waldhauser & Schaff 2008), whereas large inter-event distance is important to image velocity structure and determine relative locations for earthquakes that are located far apart.

However, we find that it is not necessary to use absolute t^* and single spectrum dt^* data for DDQ tomography of The Geysers because the measurement of more accurate spectral ratio dt^* data is not limited by inter-event distance. Figs S8 and S9 in the Supporting Information show that the quality of spectral ratio dt^* data, approximately represented by spectral ratio residual and closure error, is not affected by increased inter-event distance for event pairs separated by < 3 km, the maximum value we use here, which is large enough to extend over most of The Geysers study volume. Similar to DD velocity tomography, the inter-event distance is critical for DDQ tomography using dt^* data only. dt^* data with small inter-event distances are only sensitive to the model near the sources. If the inter-event distances are much smaller than the grid spacing, the model sensitivity can essentially be completely cancelled, resulting in no improvement in model resolution. Fig. S10 in the Supporting Information shows a series of checkerboard tests using synthetic dt^* data that have the same data distribution as our real spectral ratio dt^* data with different maximum inter-event distances of 0.5, 1, 2 and 3 km. They show a gradually increased model resolvability as the maximum inter-event distance is increased. However, there seems to be a limit to how large the maximum inter-event distance should be. Fig. S8 in the Supporting Information shows that setting the maximum inter-event distance larger than 2 km does not notably

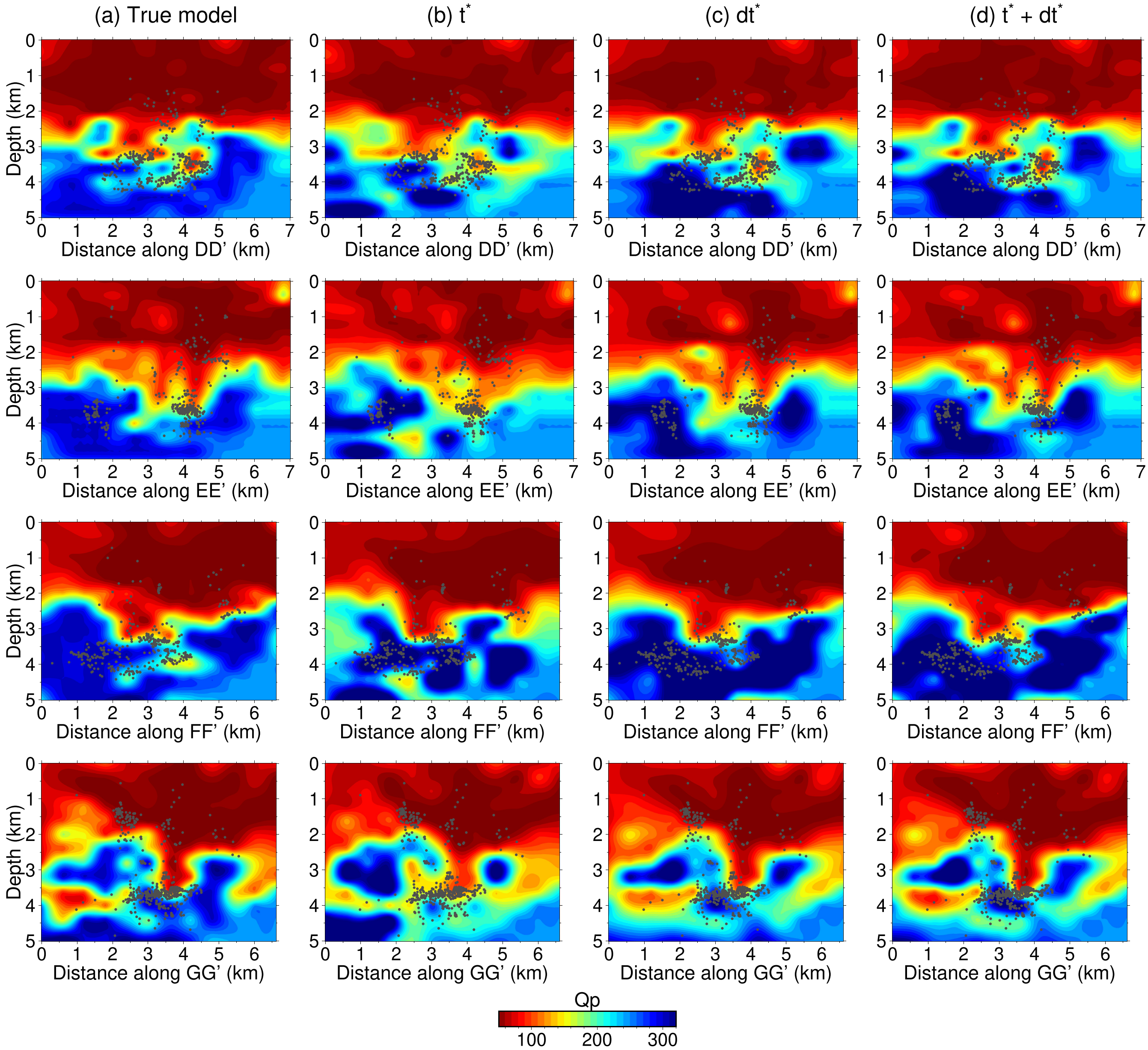

Figure 17. Cross-sections (DD′, EE′, FF′ and GG′) of the (a) input true and (b)–(d) inverted Qp models from noise-added restoration tests using (b) absolute t^* data only, (c) dt^* data only and (d) absolute t^* and dt^* data. Dots represent earthquakes within 0.3 km of each cross-section.

change the model. Thus, for The Geysers, DDQ tomography using more accurate spectral ratio dt^*data alone with maximum inter-event distance equal to or larger than ∼2 km can recover both the large- and small-scale structures well. Figs 13(b) and (c) show that the inversion combining t^* and spectral ratio dt^* data makes only a very slight difference compared to the inversion using spectral ratio dt^* data alone, which is further confirmed by checkerboard tests (Figs 14c and d and 15c and d) and restoration tests (Figs 16c and d and 17c and d). This is because the spectral ratio dt^* data of event pairs with large inter-event distances are available and can establish the large-scale structure as well as or even better than t^* data.

Although not required for DDQ tomography at The Geysers, we expect absolute t^* data and single spectrum dt^* data can be helpful in regions of larger scale and regions with earthquake sources that are not so close to the surface. Our choice of 3 km for the maximum inter-event distance of the spectral ratio dt^* data for The Geysers is suitable in terms of obtaining good model resolution at an acceptable computational cost. For larger scale regions, such as subduction zones, setting a much larger maximum inter-event distance, for example, 50 km, is probably required to recover the model well if only spectral ratio dt^* data are used. However, this may result in a huge amount of spectral ratio dt^* data being constructed, depending on the numbers of events and stations used, which can result in high computational cost for both the spectral ratio inversion and the tomographic inversion. In this case, it may be better to include absolute t^* data to establish large-scale structure and the single spectrum dt^* data with an inter-event distance of ∼30 km, for example, to constrain small-scale structures, whereas the spectral ratio dt^* data with relatively smaller inter-event distance, for example, ∼20 km, can be constructed to further refine small-scale structures in the source regions.

5.3 Interpretation of reservoir conditions of The Geysers

We divide the whole geothermal field of The Geysers into three regions. The northwest region is to the northwest of a line trending northeast passing through the point $X = 0$ km and $Y = 0$ km (horizontal distances $< \sim 7$ km in the AA′–CC′ cross-sections in Figs 11a and c). The central region is between two lines trending northeast passing through two points, one of which is $X = 0$ km and $Y = 0$ km, and the other one is $X = -2$ km and $Y = -2$ km (horizontal distances ∼7–10 km in the AA′–CC′ cross-sections in Figs 11a and c). The southeast region is to the southeast of the line trending northeast passing through the point $X = -2$ km and $Y = -2$ km (horizontal distances $> \sim 10$ km in the AA′–CC′ cross-sections in Figs 11a and c). Note that depth throughout the paper is defined relative to sea level.

Strong lateral and vertical heterogeneity of the reservoir conditions have been found beneath the entirety of The Geyser geothermal field by many previous geophysics, geology, geochemistry, hydrology, rock physics and mechanical modelling studies in the past decades (Walters *et al.* 1988; O'Connell & Johnson 1991; Zucca *et al.* 1994; Romero *et al.* 1995; Julian *et al.* 1996; Romero *et al.* 1997; Gritto *et al.* 2013; Garcia *et al.* 2016; Rutqvist *et al.* 2016; Lin & Wu 2018; Hutchings *et al.* 2019). In recent years, more attention has been paid to the northwest region, where a deep vapour-dominated high temperature reservoir (HTR, ∼300–400 °C) exists at depths below ∼2 km underneath a conventional steam reservoir of normal temperature (NTR, ∼240 °C) at depths of ∼1–2 km (Walter *et al.* 1988). An Enhanced Geothermal System (EGS) Demonstration Project has been performed in this area since 2009 (Jeanne *et al.* 2015; Garcia *et al.* 2016; Rutqvist *et al.* 2016), which aims to enhance the production from the HTR by water injection. Previous seismic velocity and attenuation tomography studies show low Vp/Vs and high attenuation anomalies at depths of ∼2–3 km in the northwest region, which may correspond to the HTR (e.g. Romero *et al.* 1995,1997; Julian *et al.* 1996; Lin & Wu 2018). Due to limited resolution at the depth of the HTR, however, it has not been well resolved by seismic tomography studies in terms of its depth range and lateral extent. The Geysers has a long history of water injection to enhance the steam production from the NTR and HTR (Hartline *et al.* 2016). High-resolution imaging of structure of water injection zones is important to understand how the injection activities have changed the reservoir conditions (Jeanne *et al.* 2015). Here, we focus on using our high-resolution earthquake relocations, Vp and Qp models to characterize the NTR, HTR and water injection zone.

The NTR extends throughout the geothermal field with varying depth range in different regions, whereas the HTR only exists in the northwest region. Northwest–southeast cross-sections and horizontal slices of the Vp and Qp models show that, at depths of ∼0.5–2 km where the NTR is located, both Vp and Qp are lowest in the southeastern part of the northwest region (Figs 11a–c and 12a–d). This zone has also been imaged as a low Vp and low Vp/Vs (1.67–1.72) zone by previous tomography studies (e.g. Julian *et al.* 1996; Lin & Wu 2018). At ∼2 km depth, there is a generally sharp transition in Vp and Qp beneath the northwest region, which can be seen from all cross-sections of different orientations crossing this region (Fig. 11). This transition well characterizes the boundary between the NTR and HTR. Below ∼2 km depth, the most prominent structure is a ∼1–2 km wide zone of low Vp and Qp in the HTR in the southeastern part of the northwest region (horizontal distances ∼4–6 km in Figs 11a–c), associated with very active seismicity. Earthquakes are relatively scattered in its upper portion, but are very concentrated and show lineations in its lower portion. The bottom of this anomaly extends to nearby regions in some cross-sections. Southwest–northeast cross-sections and north–south cross-sections also clearly show this anomaly at depths of ∼2–4 km (Figs 11d–g). Compared to this anomaly, the region further to the northwest (horizontal distances $< \sim 4$ km in Figs 11a–c) shows relatively higher Vp and Qp. Fig. 12 shows the depth slices of the Vp and Qp models relative to the mean values at each depth, which better shows the lateral extent of the anomalies seen from the cross-sections. Overall, Vp and Qp at each depth vary horizontally from the northwest to the southeast regions by ±10 per cent and ±60 per cent, respectively, with lowest Vp and Qp in the southeastern part of the northwest region. The sharp contrast in Vp and Qp between the northwest and the central regions at depths less than ∼2 km may indicate the deep extension of a local northeast-trending fault into the NTR depth range (Garcia *et al.* 2016).

Factors that influence Vp, Qp and other physical properties in the crust include lithology, fracturing, fluid versus gas saturation, effective pressure, temperature and hydration of minerals, especially for steam reservoirs in geothermal fields. The Geysers steam reservoirs lie primarily within a metagraywacke and are overlain by Franciscan greenstone melange and unfractured metagraywacke (Thompson 1992). A felsite body intruded into the base of the metagraywacke during the Pleistocene (Schriener & Suemnicht 1980) and it is suggested to have hydrothermally altered and hydraulically fractured the metagraywacke, increasing the permeability to host the present steam reservoirs (Romero *et al.* 1995). Combined with a long history of fluid injection since 1970 to sustain or enhance the reservoir pressure and the steam production, the NTR and HTR are highly fractured, with fractures filled by liquid and/or vapour (Hartline *et al.* 2016).

Our observed variations in Vp and Qp in the NTR throughout the field are too large to be the effect of temperature variation alone and must be explained by variations in fracturing, pore pressure, permeability, saturation and/or lithology (Julian *et al.* 1996). These factors have been thoroughly investigated by theoretical and lab rock physics studies (e.g. Winkler & Nur 1979; Hutchings *et al.* 2019). Two important activities, water injection and steam production, are likely responsible for these variations. Since the geothermal reservoir is naturally vapour-dominated, low Vp/Vs is expected as was imaged by Julian *et al.* (1996). In the southeastern part of the northwest region, the distribution of wells is denser than any other part of the field (Fig. 11). In high porosity rocks, the introduction of fluids into pores or fractures from the water injection activities can increase the rock density and decrease Vp, although bulk modulus is increased. Partial saturation of fluids also increases intrinsic attenuation. Water injection can also result in more fracturing that decreases Vp due to the decreased bulk modulus. More fracturing also increases intrinsic attenuation. As steam is produced continuously, steam pressure in the reservoir is decreased and thus effective stress is increased. This can result in increased velocity and decreased attenuation. Since the injected fluid can be converted to steam after encountering hot reservoir rocks, however, steam pressure can be recovered to some degree. Thus, we suggest two possible interpretations for the large northwest to southeast variations in Vp and Qp in the NTR. (1) The southeastern part of the northwest region, where both Vp and Qp are lowest, has a higher degree of fracturing, permeability, and saturation (although not fully saturated), compared to the regions to the southeast and northwest. (2) Steam pressure is significantly lower in the central and southeast regions due to steam production.

For the HTR in the northwest region, the strong variations in *Vp* and *Qp* within it may reflect variations in permeability and saturation. For the southeastern part of the HTR (horizontal distances ∼4–6 km in AA′–CC′ cross-sections in Figs 11a–c), earthquakes are concentrated at its base. As the cool water encounters hot reservoir rocks, microearthquakes are induced due to the generation of new cracks and fractures and the reactivation of existing fractures (Hartline *et al.* 2016, and references therein). Consequently, microearthquakes can be used as a proxy for pathways of fluid migration near the injection wells. Clustered earthquakes in the southeastern part of the HTR, some of which show lineations, indicate the existence of fluids in this narrow zone, which is probably due to water injection. Our imaged low *Vp* and extremely low *Qp* of this narrow zone probably indicates very high partial fluid saturation there, perhaps up to ∼ 95 per cent (Winkler & Nur 1979). This is consistent with the fact that since 2003 November, the Santa Rosa—Geysers Recharge Project has injected a large amount of tertiary-treated wastewater into this region (Stark *et al.* 2005; Majer & Peterson 2007). Another tomography study also shows that *Vp* is decreased at ∼2–3 km depths after the water injection during an EGS Demonstration Project near the northwestern edge of our study area (Jeanne *et al.* 2015). For the northwestern part of the HTR (horizontal distances < ∼4 km in AA′–CC′ cross-sections in Figs 11a–c), *Vp* and *Qp* are relatively higher, indicating much less fluid saturation or even dry fractures there (Winkler & Nur 1979). This is consistent with the inference of hot dry rocks in the HTR (Walters *et al.* 1988; Garcia *et al.* 2016).

6 CONCLUSIONS

We have developed an event-pair spectral ratio method that can solve for source and attenuation parameters using spectral ratio data from pairs of events at common stations. By taking the ratio, both the instrument and site responses are removed from the inversion. Synthetic tests show that the inversion of dt^* data using our spectral ratio method is relatively insensitive to the choice of source model (high-frequency decay factor) and is robust to a moderate amount of noise. Applying the new spectral ratio method to real *P*-wave data at The Geysers fits the data better than the standard single spectrum method, indicating that the spectral ratio dt^* data are more accurate than absolute t^* data. Before DDQ tomographic inversion, we relocated 2937 earthquakes and determined a new 3-D *Vp* model using the DD location and tomography method, with a new strategy for constructing event-pair differential time data. Both the real data inversions and synthetic tests show that DDQ tomographic inversion using spectral ratio dt^* data achieves higher resolution at The Geysers than the standard *Q* tomographic inversion using absolute t^* data, especially in zones of concentrated earthquakes. At depths of ∼0.5–2 km where a vapour-dominated NTR exists, our results reveal strong variations in *Vp* and *Qp* from the northwest to the southeast regions, which can be attributed to variations in fracturing, permeability, fluid saturation and/or steam pressure. At depths of ∼2–4 km, a prominent low-*Vp* and low-*Qp* zone is imaged within a known HTR and is probably caused by the large amount of fluids injected into this zone, which can also explain the very active induced seismicity there.

ACKNOWLEDGEMENTS

Waveform data, metadata, or data products for this study were accessed through the Northern California Earthquake Data Center, doi:10.7932/NCEDC. We thank Gritto Roland for providing event lists and Avinash Nayak for archiving waveform data. We thank two reviewers for their constructive comments that help us to improve this manuscript. This work is supported by NSF award EAR-1724685.

DATA AVAILABILITY STATEMENT

Waveform data, metadata, or data products for this study were accessed through the Northern California Earthquake Data Center (2014). The earthquake relocations and Vp and Qp models developed in this study are available in Zenodo, at https://zenodo.org/record/4470253#.YBDr1y-ZNVo. The DDQ tomography code can be made available upon request.

REFERENCES

Abercrombie, R.E., 2014. Stress drops of repeating earthquakes on the San Andreas fault at Parkfield, *Geophys. Res. Lett.,* **41**(24), 8784–8791.

Aster, R.C., Borchers, B. & Thurber, C.H., 2019. *Parameter Estimation and Inverse Problems,* Academic Press.

Bakun , W.H., 1984. Seismic moments, local magnitudes, and coda-duration magnitudes for earthquakes in central California, *Bull. seism. Soc. Am.,* **74**(2):439–458.

Bennington, N., Thurber, C. & Roecker, S., 2008. Three-dimensional seismic attenuation structure around the SAFOD site, Parkfield, California, *Bull. seism. Soc. Am.,* **98**(6), 2934–2947.

Bisrat, S.T., DeShon, H.R., Pesicek, J. & Thurber, C., 2014. High-resolution 3-DP wave attenuation structure of the New Madrid Seismic Zone using local earthquake tomography, *J. geophys. Res.: Solid Earth,* **119**(1), 409–424.

Blakeslee, S., Malin, P. & Alvarez, M., 1989. Fault-zone attenuation of high-frequency seismic waves, *Geophys. Res. Lett.,* **16**(11), 1321–1324.

Brune, J.N., 1970. Tectonic stress and the spectra of seismic shear waves from earthquakes, *J. geophys. Res.,* **75**(26), 4997–5009.

Eberhart-Phillips, D. & Chadwick, M., 2002. Three-dimensional attenuation model of the shallow Hikurangi subduction zone in the Raukumara Peninsula, New Zealand, *J. geophys. Res.: Solid Earth,* **107**(B2), doi:10.1029/2000JB000046.

Eberhart-Phillips, D., Thurber, C.H. & Fletcher, J.B., 2014. Imaging P and S Attenuation in the Sacramento–San Joaquin Delta Region, Northern California, *Bull. seism. Soc. Am.,* **104**(5), 2322–2336, doi:10.1785/0120130336.

Faul, U. & Jackson, I., 2015. Transient creep and strain energy dissipation: an experimental perspective, *Annu. Rev. Earth Planet. Sci.,* **43,** 541–569.

Frankel, A., 1991. Mechanisms of seismic attenuation in the crust: scattering and anelasticity in New York State, South Africa, and southern California, *J. geophys. Res.: Solid Earth,* **96**(B4), 6269–6289.

Garcia, J., Hartline, C., Walters, M., Wright, M., Rutqvist, J., Dobson, P.F. & Jeanne, P., 2016. The Northwest Geysers EGS demonstration project, California: Part 1: characterization and reservoir response to injection, *Geothermics,* **63,** 97–119.

Gritto, R. & Jarpe, S.P., 2014. Temporal variations of Vp/Vs-ratio at The Geysers geothermal field, USA, *Geothermics,* **52,** 112–119.

Gritto, R., Jarpe, S.P., Hutchings, L.J., Ulrich, C., Layland-Bachmann, C.E., Schoenball, M. & Nakagawa, S., 2020. Seismic imaging of spatial heterogeneity at The Geysers geothermal reservoir using a cost-effective dense seismic network, in *Proceedings, 45th Workshop on Geothermal Reservoir Engineering, SGP-TR-216,* Stanford Geothermal Program, Stanford University, Stanford, California.

Gritto, R., Yoo, S.H. & Jarpe, S.P., 2013. Three-dimensional seismic tomography at The Geysers geothermal field, CA, USA, in *Proceedings, 38th Workshop on Geothermal Reservoir Engineering, SGP-TR-198,* Stanford Geothermal Program, Stanford University, Stanford, California.

Guo, H., McGuire, J.J. & Zhang, H., 2018a. Imaging the subducted Gorda plate: Implications for the stress state and brittle-ductile transition of the Cascadia subduction zone, in *American Geophysical Union Fall Meeting 2018,* T13H-0334, American Geophysical Union.

Guo, H. & Zhang, H., 2017. Development of double-pair double difference earthquake location algorithm for improving earthquake locations, *Geophys. J. Int.,* **208**(1), 333–348.

Guo, H., Zhang, H. & Froment, B., 2018b. Structural control on earthquake behaviors revealed by high-resolution Vp/Vs imaging along the Gofar transform fault, East Pacific Rise, *Earth planet. Sci. Lett.,* **499,** 243–255.

Hartline, C.S., Walters, M.A., Wright, M.C., Forson, C.K. & Sadowski, A.J., 2016. Three-dimensional structural model building, induced seismicity analysis, drilling analysis, and reservoir management at The Geysers Geothermal Field, Northern California, in *Proceedings, 41st Workshop on Geothermal Reservoir Engineering, SGP-TR-209,* Stanford Geothermal Program, Stanford University, Stanford, California.

Hutchings, L., Bonner, B., Saltiel, S., Jarpe, S. & Nelson, M., 2019. Rock physics interpretation of tomographic solutions for geothermal reservoir properties, in *Applied Geophysics with Case Studies on Environmental, Exploration and Engineering Geophysics*. Ali Ismet Kanlı, IntechOpen, doi:10.5772/intechopen.81226.

Imanishi, K. & Ellsworth, W.L., 2006. Source scaling relationships of microearthquakes at Parkfield, CA, determined using the SAFOD pilot hole seismic array, *GMS,* **170,** 81–90.

Jeanne, P., Rutqvist, J., Hutchings, L., Singh, A., Dobson, P.F., Walters, M. & Garcia, J., 2015. Degradation of the mechanical properties imaged by seismic tomography during an EGS creation at The Geysers (California) and geomechanical modeling, *Phys. Earth planet. Inter.,* **240,** 82–94.

Johnson, L.R., 2014. Source mechanisms of induced earthquakes at The Geysers geothermal reservoir, *Pure appl. Geophys.,* **171**(8), 1641–1668.

Julian, B.R., Ross, A., Foulger, G.R. & Evans, J.R., 1996. Three-dimensional seismic image of a geothermal reservoir: The Geysers, California, *Geophys. Res. Lett.,* **23**(6), 685–688.

Kriegerowski, M., Cesca, S., Ohrnberger, M., Dahm, T. & Krüger, F., 2019. Event couple spectral ratio Q method for earthquake clusters: application to North-West Bohemia, *Solid Earth,* **10,** 317–328.

Lin, G., 2015. Seismic velocity structure and earthquake relocation for the magmatic system beneath Long Valley Caldera, eastern California, *J. Volc. Geotherm. Res.* **296,** 19–30.

Lin, G. & Wu, B., 2018. Seismic velocity structure and characteristics of induced seismicity at the Geysers geothermal field, eastern California, *Geothermics,* **71,** 225–233.

Liu, X., Zhao, D. & Li, S., 2014. Seismic attenuation tomography of the Northeast Japan arc: insight into the 2011 Tohoku earthquake (Mw 9.0) and subduction dynamics, *J. geophys. Res.: Solid Earth,* **119**(2), 1094–1118.

Maeda, N., 1985. A method for reading and checking phase times in autoprocessing system of seismic wave data, *ZisinJishin,* **38,** 365–379.

Majer, E.L. & Peterson, J.E., 2007. The impact of injection on seismicity at The Geysers, California Geothermal Field, *Int. J. Rock Mech. Min. Sci.,* **44**(8), 1079–1090.

NCEDC, 2014. Northern California Earthquake Data Center. UC Berkeley Seismological Laboratory. Dataset. doi:10.7932/NCEDC.

O'Connell, D.R. & Johnson, L.R., 1991. Progressive inversion for hypocenters and P wave and S wave velocity structure: application to the Geysers, California, geothermal field, *J. geophys. Res.: Solid Earth,* **96**(B4), 6223–6236.

O'Connell, R.J. & Budiansky, B., 1977. Viscoelastic properties of fluid-saturated cracked solids, *J. geophys. Res.,* **82**(36), 5719–5735.

Ohlendorf, S., Thurber, C., Prejean, S. & Pesicek, J., 2014. Seismicity and seismic structure at Okmok volcano, Alaska, *J. Volc. Geotherm. Res.,* **278–279,** 103–119.

Paige, C.C. & Saunders, M.A., 1982. LSQR: an algorithm for sparse linear equations and sparse least squares, *ACM Trans. Math. Softw. (TOMS),* **8**(1), 43–71.

Peacock, S., McCann, C., Sothcott, J. & Astin, T.R., 1994. Experimental measurements of seismic attenuation in microfractured sedimentary rock, *Geophysics,* **59**(9), 1342–1351.

Pesicek, J.D., Bennington, N.L., Thurber, C.H. & Zhang, H., 2011. Improving attenuation tomography by novel inversions for t∗ and Q: application to Parkfield, California and Okmok volcano, Alaska, in *AGUFM,* S41A–2173, American Geophysical Union.

Pozgay, S.H., Wiens, D.A., Conder, J.A., Shiobara, H. & Sugioka, H., 2009. Seismic attenuation tomography of the Mariana subduction system: Implications for thermal structure, volatile distribution, and slow spreading dynamics, *Geochem. Geophys. Geosyst.,* **10**(4), doi:10.1029/2008GC002313.

Rietbrock, A., 1996. *Entwicklung eines Programmsystems zure konsistenten Auswertung grober seismologischer Datensatze mit Anwendung auf die Untersuchung der Absorptions-struktur der Loma-Prieta-Region Kalifornien (Development of an interactive analysis system for large seismological data sets; application to the determination of the absorption structure in the Loma Prieta region, California)*. Ph.D. dissertation, Ludwig-Maximulians-Universitat Munchen, Munich, Germany, p. 143.

Rietbrock, A., 2001. P wave attenuation structure in the fault area of the 1995 Kobe earthquake, *J. geophys. Res.: Solid Earth,* **106**(B3), 4141–4154.

Romero, A.E., Jr, McEvilly, T.V. & Majer, E.L., 1997. 3-D microearthquake attenuation tomography at the Northwest Geysers geothermal region, California, *Geophysics,* **62**(1), 149–167.

Romero, A.E., Jr, McEvilly, T.V., Majer, E.L. & Vasco, D., 1995. Characterization of the geothermal system beneath the Northwest Geysers steam field, California, from seismicity and velocity patterns, *Geothermics,* **24**(4), 471–487.

Roth, E.G., Wiens, D.A., Dorman, L.M., Hildebrand, J. & Webb, S.C., 1999. Seismic attenuation tomography of the Tonga-Fiji region using phase pair methods, *J. geophys. Res.: Solid Earth,* **104**(B3), 4795–4809.

Rutqvist, J., Jeanne, P., Dobson, P.F., Garcia, J., Hartline, C., Hutchings, L. & Walters, M., 2016. The Northwest Geysers EGS demonstration project, California–part 2: modeling and interpretation, *Geothermics,* **63,** 120–138.

Sato H., Fehler M.C., 2009, Seismic Wave Propagation and Scattering in the Heterogeneous Earth, Berlin: Springer, doi:10.1007/978-3-540-89623-4.

Scherbaum, F., 1990. Combined inversion for the three-dimensional Q structure and source parameters using microearthquake spectra, *J. geophys. Res.: Solid Earth,* **95**(B8), 12423–12438.

Schriener, A., Jr & Suemnicht, G.A., 1980. Subsurface intrusive rocks at The Geysers geothermal area, California, in *Proceedings of Symposium Miner Deposition Pacific Northwest,* Silberman *et al*., eds, USGS Open File Report 81–355, pp. 294–303.

Shiina, T., Nakajima, J. & Matsuzawa, T., 2018. P-wave attenuation in the Pacific slab beneath northeastern Japan revealed by the spectral ratio of intraslab earthquakes, *Earth planet. Sci. Lett.,* **489,** 37–48.

Stark, M.A., Box, W.T., Jr, Beall, J.J., Goyal, K.P. & Pingol, A.S., 2005. The Santa Rosa–Geysers recharge project, Geysers geothermal field, California, USA, in *Proc. World Geotherm. Cong,* ed. Horne, R.N.., International Geothermal Association.

Thompson, R.C., 1992. Structural stratigraphy and intrusive rocks at The Geysers geothermal field, in *Monograph on The Geysers Geothermal Field, Special Report No. 17,* pp. 59–63, ed. Stone C., Geothermal Resources Council.

Thomson, D.J., 1982. Spectrum estimation and harmonic analysis, *Proc. IEEE,* **70**(9), 1055–1096.

Thurber, C.H. & Eberhart-Phillips, D., 1999. Local earthquake tomography with flexible gridding, *Comput. Geosci.,* **25**(7), 809–818, doi:10.1016/S0098-3004(99)00007-2.

Waldhauser, F., 2001. hypoDD—a program to compute double-difference hypocenter locations, USGS Open File Rep., 01–113.

Waldhauser, F. & Ellsworth, W.L., 2000. A double-difference earthquake location algorithm: method and application to the northern Hayward fault, California, *Bull. seism. Soc. Am.,* **90**(6), 1353–1368.

Waldhauser, F. & Schaff, D.P., 2008. Large-scale relocation of two decades of Northern California seismicity using cross-correlation and double-difference methods, *J. geophys. Res.: Solid Earth,* **113**(B8), doi:10.1029/2007JB005479.

Walters, M.A., Sternfeld, J.N., Haizlip, J.R., Drenick, A.F. & Combs, J., 1988. A vapor-dominated reservoir exceeding 600° F at The Geysers, Sonoma County, California, in *Proceedings, 13th Workshop on Geothermal Reservoir Engineering, SGP-TR-113,* Stanford Geothermal Program, Stanford University, Stanford, California.

Wei, S.S. & Wiens, D.A., 2018. P-wave attenuation structure of the Lau back-arc basin and implications for mantle wedge processes, *Earth planet. Sci. Lett.,* **502,** 187–199.

Winkler, K. & Nur, A., 1979. Pore fluids and seismic attenuation in rocks, *Geophys. Res. Lett.,* **6**(1), 1–4.

Yu, H., Harrington, R.M., Kao, H., Liu, Y., Abercrombie, R.E. & Wang, B., 2020. Well proximity governing stress drop variation and seismic attenuation associated with hydraulic fracturing induced earthquakes, *J. geophys. Res.: Solid Earth,* **125**(9), doi:10.1029/2020JB020103.

Zelt, C.A., 1998. Lateral velocity resolution from three-dimensional seismic refraction data, *Geophys. J. Int.,* **135**(3), 1101–1112.

Zhang, H., Liu, Y., Thurber, C.H., Xu, Z. & Song, X., 2007. High-resolution seismic velocity and attenuation structure of the Sichuan-Yunnan region, Southwest China, using seismic catalog and waveform data. Final report, accession number: ADA472285.

Zhang, H. & Thurber, C.H., 2003. Double-difference tomography: the method and its application to the Hayward fault, California, *Bull. seism. Soc. Am.,* **93**(5), 1875–1889.

Zucca, J.J., Hutchings, L.J. & Kasameyer, P.W., 1994. Seismic velocity and attenuation structure of the Geysers geothermal field, California, *Geothermics,* **23**(2), 111–126.

SUPPORTING INFORMATION

Supplementary data are available at *GJI* online.

Figure S1. The evolution of inverted dt^* with iterations for (a)–(c) noise-free and (d)–(f) noise-added synthetic tests that generate synthetic spectral ratio data with γ values of (a) and (d) 2, (b) and (e) 1.5 and (c) and (f) 2.5 and use a γ value of 2 for inversions. All the other elements are the same as that of Fig. 2. Compared to the results shown in Fig. 2, the results in this figure are from the synthetic tests setting more different true f_c values for the two events.

Figure S2. Trade-off curve analysis for the selection of optimal regularization parameters used for *Vp* tomography. (a) Selecting damping. Three lines represent the results from the inversions using smoothing values of 10, 20 and 30. Dots on each line represent the results from the inversions using the same smoothing but different damping values labelled by their adjacent numbers. The damping value we selected for *Vp* tomography is 400 with slight variations for different iterations to maintain the desired condition number of the inversion system. (b) Selecting smoothing. The line connects the results from the inversion using the damping value of 400 and different smoothing values from 1 to 1000 as indicated. The smoothing value we selected is 20.

Figure S3. Noise-free checkerboard resolution test for Vp tomography. (a), (c) and (e) True *Vp* model and (b), (d) and (f) inverted *Vp* model along the cross-sections at $X = -2$, -1.4 and -0.8 km. Black lines in (b), (d) and (f) approximately outline the regions that are well recovered.

Figure S4. Spectral ratio inversion results for two example event pairs. All the elements in this figure are the same as that in Fig. 9 but for two different event pairs. For the two events shown in (a) and (b), their magnitudes are 1.4 and 1.3, their depths are 4.11 and 3.67 km, the distance between them is 1.97 km, and their inverted f_c values are 12.0 and 13.2 Hz. For the two events shown in (c) and (d), their magnitudes are 1.2 and 1.4, their depths are 3.07 and 1.44 km, and the distance between them is 2.10 km, and their inverted f_c values are 14.7 and 12.5 Hz.

Figure S5. (a) Histogram of all f_c estimates for one example event. (b) Histogram of the mean of all f_c estimates for all events.

Figure S6. Seismic moment versus f_c for (a) all the earthquakes we used and (b)–(d) the earthquakes at different depth ranges. Each blue dot represents the result of an earthquake with a horizontal bar showing the uncertainty of the estimated f_c. The uncertainty of the estimated f_c of each earthquake is the standard deviation of its f_c estimates from spectral ratio inversions of all of its event pairs. Solid lines denote iso-value lines of static stress drops at 0.01, 0.1, 1, 10 and 100 MPa. The seismic moments are converted from the local magnitudes in Northern California Earthquake Data Center catalogue (2014) based on the seismic moment versus local magnitude relation determined by Bakun (1984). The red line is the scaling relation determined by Johnson (2014) using source properties of 20 earthquakes estimated by a dynamic moment tensor method.

Figure S7. Histogram of closure errors of dt^* data. The final closure error of each dt^* is the average of absolute values of all its associated individual closure error measurements.

Figure S8. Inter-event distances versus final spectral ratio residuals for all event pairs. Colour represents the number of data points in each small area.

Figure S9. Inter-event distances versus closure errors for dt^* data. The final closure error of each dt^* is the average of absolute values of all its associated individual closure error measurements. Only the dt^* data that have at least 50 individual closure error measurements are used for this figure. Colour represents the number of data points in each small area.

Figure S10. Checkerboard resolution tests of DDQ tomography using the synthetic dt^* data with different maximum inter-event distances (0.5, 1, 2 and 3 km). Different rows correspond to different cross-sections. Black lines outline the well recovered regions in each cross-section.

Please note: Oxford University Press is not responsible for the content or functionality of any supporting materials supplied by the authors. Any queries (other than missing material) should be directed to the corresponding author for the paper.